Cell

Resource

Single-cell dissection of the human motor and prefrontal cortices in ALS and FTLD

Graphical abstract

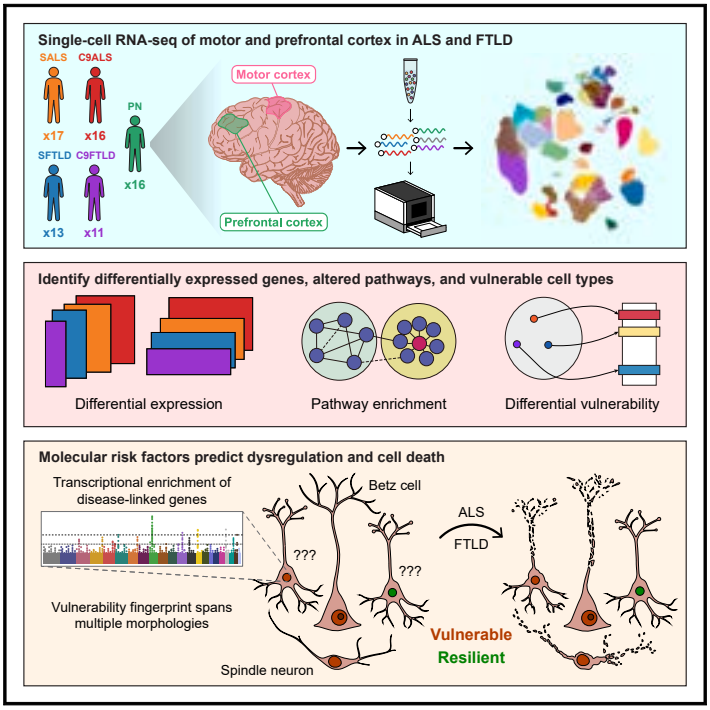

Highlights

- Multi-region atlas of 625,973 cells from 73 ALS, FTLD, and control individuals
- Alterations in sporadic and *C9orf72*+ familial cases are highly convergent
- Highly affected cell types are enriched for known genetic risk factors
- Vulnerability fingerprint transcends brain regions and canonical cell types

Authors

S. Sebastian Pineda, Hyeseung Lee, Maria J. Ulloa-Navas, ..., Myriam Heiman, Veronique V. Belzil, Manolis Kellis

Correspondence

mheiman@mit.edu (M.H.), veronique.belzil@vumc.org (V.V.B.), manoli@mit.edu (M.K.)

In brief

Cell-type-specific transcriptional changes across the ALS-FTLD disease spectrum are studied through an integrated single-cell atlas of the human motor and prefrontal cortices, revealing molecular fingerprints and disease signatures of vulnerable cell types as well as non-cell-autonomous pathological mechanisms.

Pineda et al., 2024, Cell *187*, 1971–1989
April 11, 2024
https://doi.org/10.1016/j.cell.2024.02.031

CellPress

Cell

CellPress

Resource

Single-cell dissection of the human motor and prefrontal cortices in ALS and FTLD

S. Sebastian Pineda,[1,2,3,4] Hyeseung Lee,[3] Maria J. Ulloa-Navas,[5] Raleigh M. Linville,[3,4] Francisco J. Garcia,[3,6] Kyriakitsa Galani,[2,4] Erica Engelberg-Cook,[5] Monica C. Castanedes,[5] Brent E. Fitzwalter,[3] Luc J. Pregent,[5] Mahammad E. Gardashli,[5] Michael DeTure,[5] Diana V. Vera-Garcia,[5] Andre T.S. Hucke,[5] Bjorn E. Oskarsson,[7] Melissa E. Murray,[5] Dennis W. Dickson,[5] Myriam Heiman,[3,6,9,*] Veronique V. Belzil,[5,8,*] and Manolis Kellis[1,2,4,*]

[1]Department of Electrical Engineering and Computer Science, Massachusetts Institute of Technology, Cambridge, MA 02139, USA
[2]Computer Science and Artificial Intelligence Laboratory, Massachusetts Institute of Technology, Cambridge, MA 02139, USA
[3]Picower Institute for Learning and Memory, Massachusetts Institute of Technology, Cambridge, MA 02139, USA
[4]Broad Institute of MIT and Harvard, Cambridge, MA 02141, USA
[5]Department of Neuroscience, Mayo Clinic, Jacksonville, FL 32224, USA
[6]Department of Brain and Cognitive Sciences, Massachusetts Institute of Technology, Cambridge, MA 02139, USA
[7]Department of Neurology, Mayo Clinic, Jacksonville, FL 32224, USA
[8]Present address: Department of Neurology, Vanderbilt University Medical Center, Nashville, TN 37232, USA
[9]Lead contact
*Correspondence: mheiman@mit.edu (M.H.), veronique.belzil@vumc.org (V.V.B.), manoli@mit.edu (M.K.)
https://doi.org/10.1016/j.cell.2024.02.031

SUMMARY

Amyotrophic lateral sclerosis (ALS) and frontotemporal lobar degeneration (FTLD) share many clinical, pathological, and genetic features, but a detailed understanding of their associated transcriptional alterations across vulnerable cortical cell types is lacking. Here, we report a high-resolution, comparative single-cell molecular atlas of the human primary motor and dorsolateral prefrontal cortices and their transcriptional alterations in sporadic and familial ALS and FTLD. By integrating transcriptional and genetic information, we identify known and previously unidentified vulnerable populations in cortical layer 5 and show that ALS- and FTLD-implicated motor and spindle neurons possess a virtually indistinguishable molecular identity. We implicate potential disease mechanisms affecting these cell types as well as non-neuronal drivers of pathogenesis. Finally, we show that neuron loss in cortical layer 5 tracks more closely with transcriptional identity rather than cellular morphology and extends beyond previously reported vulnerable cell types.

INTRODUCTION

Although amyotrophic lateral sclerosis (ALS) and frontotemporal lobar degeneration (FTLD) are considered two distinct diagnoses, they show overlapping clinical, pathological, and genetic characteristics, suggesting that they are part of the same disease spectrum.[1] Clinically, 40%–50% of patients diagnosed with either ALS or frontotemporal dementia (FTD) eventually develop symptoms of the other disease, and up to 15% of patients receive both diagnoses.[2–6] Pathologically, nuclear depletion and cytoplasmic accumulation of transactive response DNA binding protein of 43 kDa (TDP-43) is observed in more than 95% of ALS and ~50% of FTLD patients,[7,8] the latter known as TDP-43-associated FTLD (FTLD-TDP, hereafter FTLD). Moreover, these diseases have shared genetic underpinnings, with the most commonly known causal mutation being a hexanucleotide (G_4C_2) repeat expansion in the *C9orf72* gene.[9–11]

ALS and FTLD may also share vulnerabilities in related cell types. ALS is characterized by a progressive loss of motor neurons.[12] Although there is debate as to which motor neurons display the primary causal pathology in ALS, the earliest pathology has been observed in both spinal lower motor neurons (LMNs) and cortical upper motor neurons (UMNs).[13] UMNs in the primary motor cortex (MCX) are essential for voluntary motor control, sending intratelencephalic, extrapyramidal, and pyramidal tract projections to control the orientation, extent, and speed of movement. ALS shows loss of pyramidal tract UMNs in layer 5 (L5) of the MCX, including the morphologically distinct giant Betz cells, which make direct corticospinal connections to the LMNs.[14,15]

The dorsolateral prefrontal cortex (DLPFC) is involved in executive cognitive processes, such as working memory, attention, abstract reasoning, and motor planning. FTLD shows loss of large fork cells and von Economo neurons (VENs, sometimes called spindle neurons), which mainly reside in L5 of the anterior cingulate cortex (ACC), the frontal insula (FI), the DLPFCs (Brodmann areas 9 and 10) to a lesser extent, and potentially other brain regions.[16–19] VENs reportedly share molecular markers with UMNs,[20] and recent studies suggest that VENs may also be extratelencephalic (ET) projection neurons.[21]

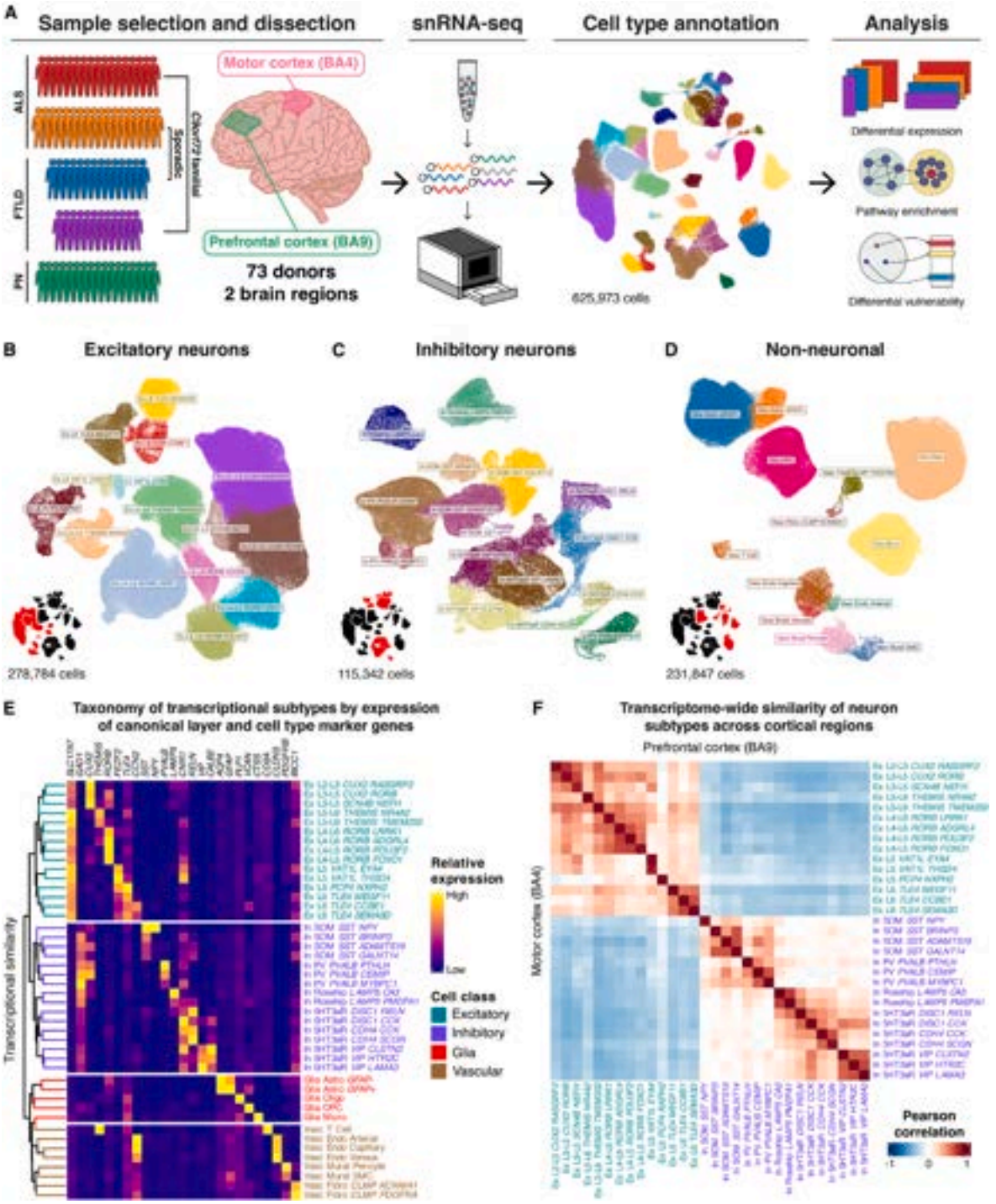

(legend on next page)

Given the selective vulnerability and rarity of these implicated cell types,[18,22,23] single-cell methods are needed to better study them. Using single-nucleus RNA sequencing (snRNA-seq) we generated comparative, single-cell molecular atlases of the MCX and DLPFC in ALS and FTLD, spanning 73 sporadic and *C9orf72* familial (C9) patients and pathologically normal (PN) controls. We use these to identify and characterize known and novel vulnerable populations, examine transcriptional alterations in neuronal, glial, and vascular cell types, identify convergent and divergent disease mechanisms and pathways across cell types, diseases, and brain regions, and implicate drivers of cell-type-specific differential vulnerability.

RESULTS

Experimental design and characterization of cell types in the affected cortices

We assembled a well-genotyped cohort of 73 donors spanning 33 ALS (17 sporadic [SALS], 16 *C9orf72* familial [C9ALS]), 24 FTLD (13 sporadic [SFTLD], 11 *C9orf72* familial [C9FTLD]), and 16 PN controls. From each donor, we obtained dissections from the MCX (Brodmann area 4; BA4) and the DLPFC (Brodmann area 9; BA9; hereafter "PFC"). From these, we isolated nuclei and generated gene expression libraries for high-throughput sequencing (Figures 1A and S1A; Table S1; STAR Methods). We report 625,973 high-quality single-nucleus profiles across 145 samples (Figure S1B; STAR Methods). We annotated 44 transcriptionally distinct subpopulations classified into excitatory and inhibitory neurons, glial, and vascular (and immune) cell types (Figures 1B–1D and S1C). We used a set of well-curated canonical layer and cell-type marker genes[24,25] (Figures 1E and S1D) to identify major known populations, which were further partitioned into transcriptional subtypes based on well-defined gene co-expression domains (Figure S1E; STAR Methods), all of which were reproducible across donors, sexes, and diseases (Figures S1F–S1I).

Translaminar L2-5 pyramidal neurons comprised the largest excitatory population and contained a notable subpopulation expressing L3-5 markers that possessed the highest expression of long-range projection markers *NEFH* and *SCN4B* (*Ex L3-L5 SCN4B NEFH*; Figures 1B, 5A, and 5B; Table S2), which may be a previously hypothesized human-specific pyramidal subtype with long-range cortico-cortical projections.[26] Of key importance were populations of L5 cells (*Ex L5 VAT1L EYA4/THSD4*) that encompass motor and spindle neurons known to be differentially vulnerable in ALS or FTLD. We captured all major classes of neocortical inhibitory neurons (Figure 1C), including subtypes of somatostatin (SOM)+ GABAergic interneurons, representing Martinotti, small basket, and long-range projecting interneurons, parvalbumin (PV)+ basket and chandelier cells, 5-HT3aR+ serotonergic interneurons, and *LAMP5*+ rosehip neurons.[27] We recovered all expected classes of glia, including oligodendrocytes, oligodendrocyte progenitors (OPC), microglia, and two astrocyte subtypes: high *GFAP*-expressing and CD44+ interlaminar and fibrous astrocytes (Astro *GFAP*+) and low *GFAP*-expressing and *CD44*− protoplasmic astrocytes (Astro *GFAP*−). Lastly, we annotated arterial, venous, and capillary subtypes of endothelial cells, smooth muscle and pericyte mural cells, fibroblasts, and CD8+ T cells (Figure 1D). *De-novo*-identified marker genes for all subtypes are provided in Table S2. Our integrated analysis produced a near-perfect overlap of transcriptionally analogous cells originating from each region, and a cross-region comparison of neuronal transcriptome-wide gene expression produced a one-to-one correspondence between most subtypes (Figure 1F), suggesting strong conservation of cell-type identity at the transcriptional level but with potentially disease-relevant distinctions in L5 (Figures 1F and S1J). To facilitate integration and comparison with previously published datasets, we provide alternative cell-type annotations in the annotated data (Figure S1K; see STAR Methods).

Global gene expression changes in ALS and FTLD

To guide the investigation of cell-type-specific disease behavior, we performed a correlation analysis of transcriptome-wide gene expression changes, revealing four distinct global patterns of dysregulation across our cohort (Figure 2A): (1) intra-region, intra-phenotype gene expression changes were well conserved across cell types (e.g., PFC SFTLD vs. PFC C9FTLD); (2) cross-region, intra-phenotype gene expression changes were still conserved across cell types (e.g., PFC FTLD vs. MCX FTLD), but intra-cell-type correlations (along the diagonal) were weaker than those within the same region. This implies that broad, non-cell-type-specific expression changes are conserved across brain regions, but the cell-type-specific disease response is more region specific; (3) there is almost no overlap in disease signatures when comparing ALS with FTLD across different brain regions (e.g., MCX FTLD vs. PFC ALS); and (4) in contrast with (3), intra-region, cell-type-specific alterations across ALS and FTLD are conserved (e.g., diagonals of MCX ALS vs. MCX FTLD). This is exemplified by the strong cross-phenotype off-diagonals visible within each region block but absent across regions. This suggests that the cell-type-specific component of the transcriptional disease response is similar across ALS and FTLD in most cell types irrespective of genotype. Within a disease group (e.g., MCX C9FTLD), we see additional substructure indicating a shared dysregulation profile among most excitatory neurons, but with distinctions in potentially disease-relevant subtypes, most prominently among FTLD cases (Figure 2A inset).

Figure 1. Experimental design and characterization of cell types in the affected cortices

(A) Experimental design for transcriptional profiling of 73 ALS, FTLD, and PN individuals (625,973 cells).

(B–D) UMAP subplots of annotated (B) excitatory neurons, (C) inhibitory neurons, and (D) non-neuronal subtypes. Insets: clusters of full UMAP visualized in each subplot.

(E) Taxonomy of annotated subtypes. Values represent average log-transformed marker expression normalized to a maximum per column.

(F) Transcriptional similarity of neuronal populations across brain regions.

See Figure S1.

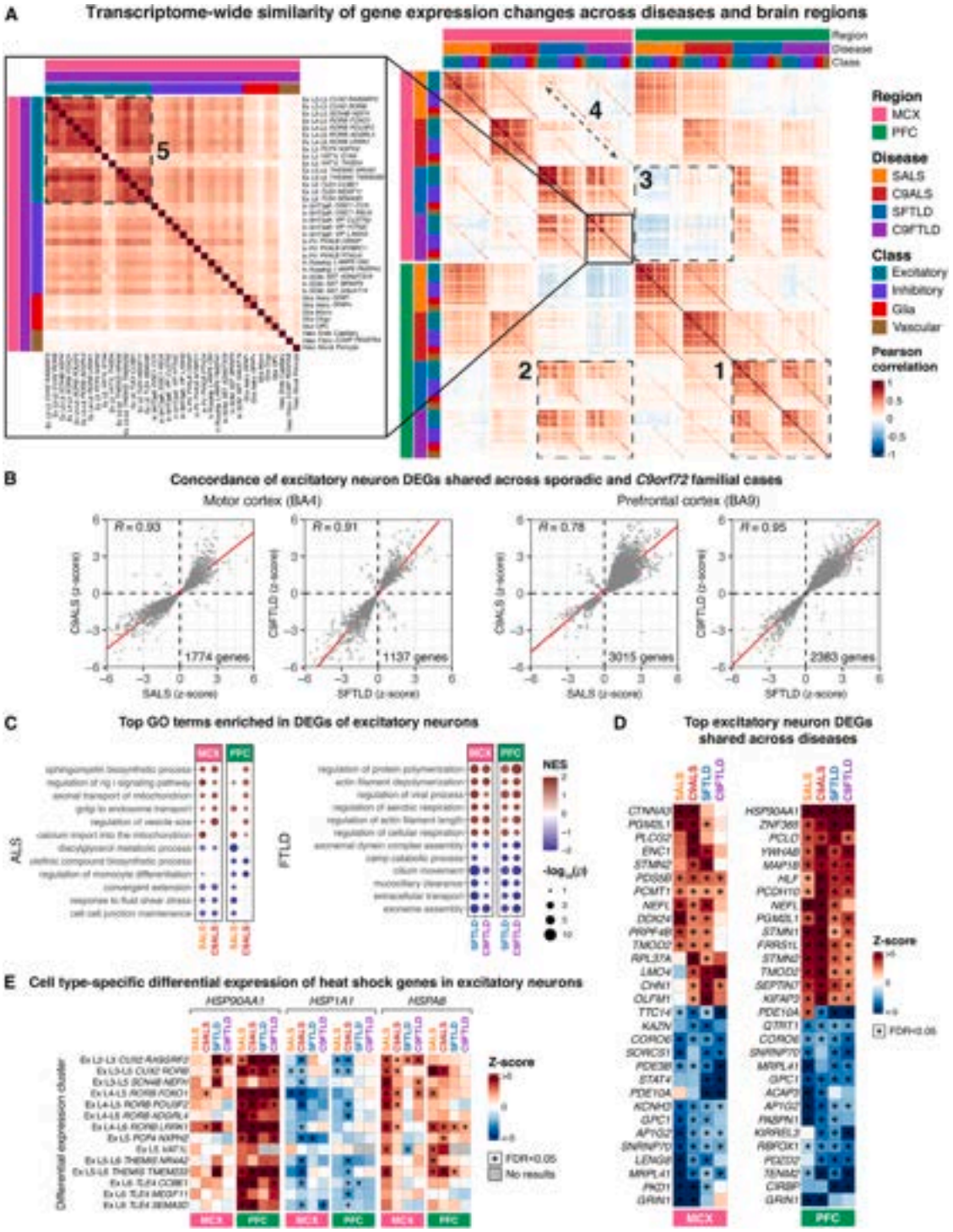

(legend on next page)

To identify genes and pathways involved in disease pathobiology, we performed two types of differential gene expression analyses across the four disease groups: (1) a coarse analysis aimed at identifying drivers of the pan-neuronal expression patterns discussed above, considering excitatory and inhibitory neuron populations each in whole, and (2) a cell-type-specific analysis focusing on individual subtypes. Details on each, including how subtypes were aggregated for analysis, can be found in Figure S1L, Table S3, and STAR Methods. The full results of all analyses can be found on Synapse (see data and code availability).

There have been conflicting reports regarding the similarity between sporadic and C9 ALS/FTLD gene expression changes.[28–30] Our pan-neuronal analysis shows exceptional gene-level similarity across genotypes in neurons of both diseases in the predominantly affected brain regions (Figures 2B and S2A). This is consistent with the fact that, without genotype information, sporadic and C9 cases of ALS and FTLD are often clinically indistinguishable. Gene set enrichment analysis (GSEA)[31] of differentially expressed genes (DEGs) upregulated in excitatory neurons of ALS cases showed enrichment of gene ontology (GO) biological process terms associated with mitochondrial and endosome transport (Figure 2C). Additionally, genes linked to sphingomyelin biosynthetic processes were upregulated in ALS (Figure 2C). This is noteworthy because overactivity of serine palmitoyltransferase (SPT), a key enzyme in sphingomyelin synthesis, has been linked to a childhood-onset, monogenic form of ALS.[32] Among upregulated FTLD DEGs in excitatory neurons, there was an enrichment for terms associated with respiration and metabolic stress (Figure 2C). Downregulated genes in FTLD were enriched for terms related to cilium function and structure (Figure 2C). Across all neurons, and in both phenotypes and brain regions, we observed a strong positive enrichment of several terms associated with cytoplasmic translation and innate immune activation (Figures 2C and S2B).

We found known ALS-linked genes neurofilament light chain (*NEFL)* and *STMN2* to be among the most upregulated excitatory neuron DEGs (Figure 2D). *NEFL* is a blood and cerebrospinal fluid (CSF) biomarker of axon degeneration in ALS and FTLD,[33] and *STMN2*, a key regulatory target of TDP-43, is essential for motor neuron axonal outgrowth and regeneration. *TTC14*, a gene encoding an RNA-binding protein linked to various ciliopathies, is among the most downregulated in the MCX (Figure 2D). We also note a pan-phenotypic downregulation of the ALS-linked gene, *PABPN1*, whose expression reportedly suppresses TDP-43 toxicity (Figures 2D and S2C).[34] The most upregulated pan-phenotypic DEG in PFC was *HSP90AA1* (Figures 2D and S2C), which encodes the inducible component of Hsp90, whose overexpression facilitates the accumulation of toxic aggregates in numerous neurodegenerative disorders, including TDP-43 and poly(GR) in ALS and FTLD.[35]

We were interested to see if any cell type was responsible for driving the dramatic upregulation of *HSP90AA1* across diseases. Cell-type-level DEG analysis revealed a pan-phenotypic upregulation of *HSP90AA1* across neuronal subtypes, primarily in the PFC (Figures 2E and S2D). Hsp90 regulates the activity of HSF-1, the master regulator of the heat shock response; therefore, we found it likely that other heat shock proteins might also be dysregulated. Indeed, we found *HSP1A1* and *HSPA8* (which encodes Hsp70) to also be dysregulated in numerous cell types, but not in the way we expected. *HSP1A1* was broadly downregulated, mainly in C9ALS, in both regions, and *HSPA8* was broadly upregulated in both regions, but more so in ALS. Lastly, we checked if *HSP90AA1* upregulation was accompanied by upregulation of immediate early genes (IEGs) because this could reflect a stress signature seen in low-quality or hypoxic cells or samples. We did not observe IEG or hypoxic signature gene upregulation in any disease group.

Non-neuronal disease mechanisms

Several studies have highlighted the important contribution of glia to ALS and FTLD disease mechanisms,[36–39] such as increased microglia and astrocyte inflammatory and immune-related gene expression, as well as decreased oligodendrocyte gene expression. We noted downregulation of astrocytic genes that contribute to neuronal homeostasis, including *SLC1A2*, *SLC4A4*, and *PTGDS*, and upregulation of zinc ion membrane transporters *SLC39A11* and *SLC39A12* (Figure 3A). These changes likely reflect shifts in astrocytic homeostatic support of neuronal metabolic function, but it is unclear if these are responsive mechanisms or causal pathogenic shifts. We noted strong positive enrichment of GO terms related to oxidative phosphorylation (OXPHOS) and protein synthesis in *GFAP*+ astrocytes of ALS MCX (Figure S2E), and in *GFAP*− astrocytes in ALS PFC (Figure S2F). These results suggest that protoplasmic astrocytes show more metabolic dysregulation in the context of the PFC, interlaminar or fibrous astrocytes in the context of the MCX, and both more so in ALS than FTLD.

We detected some upregulation of activated glia markers in astrocytes (Figure 3B) but did not observe the broad upregulation of pan-reactive, A1-reactive, or A2-reactive astroglial markers[40] nor the disease-associated or reactive astrocyte

Figure 2. Global gene expression changes in ALS and FTLD

(A) Similarity of disease-induced gene expression changes across the profiled cohort. Examples of (1) conserved intra-phenotype, intra-region alterations within and across cell types, (2) conserved intra-phenotype, cross-region alterations within and across cell types, (3) non-conservation of changes across dissimilar phenotypes and brain regions, (4) conserved cross-phenotype, intra-region alterations predominantly within cell types, and (5) conserved gene expression changes across excitatory neurons within a single phenotype and brain region.

(B) Comparison of excitatory neuron DEGs across genotypes. In each panel, the Pearson correlation is shown in the top-left and the number of overlapping DEGs (FDR < 0.05 in both genotypes) is shown in the bottom-right.

(C) Select top-ranking GO terms enriched in DEGs of excitatory neurons in ALS and FTLD cases.

(D) Top up- and downregulated genes shared across diseases in excitatory neurons, per brain region.

(E) Differential expression of heat shock genes broadly dysregulated across excitatory neurons.

See Figure S2.

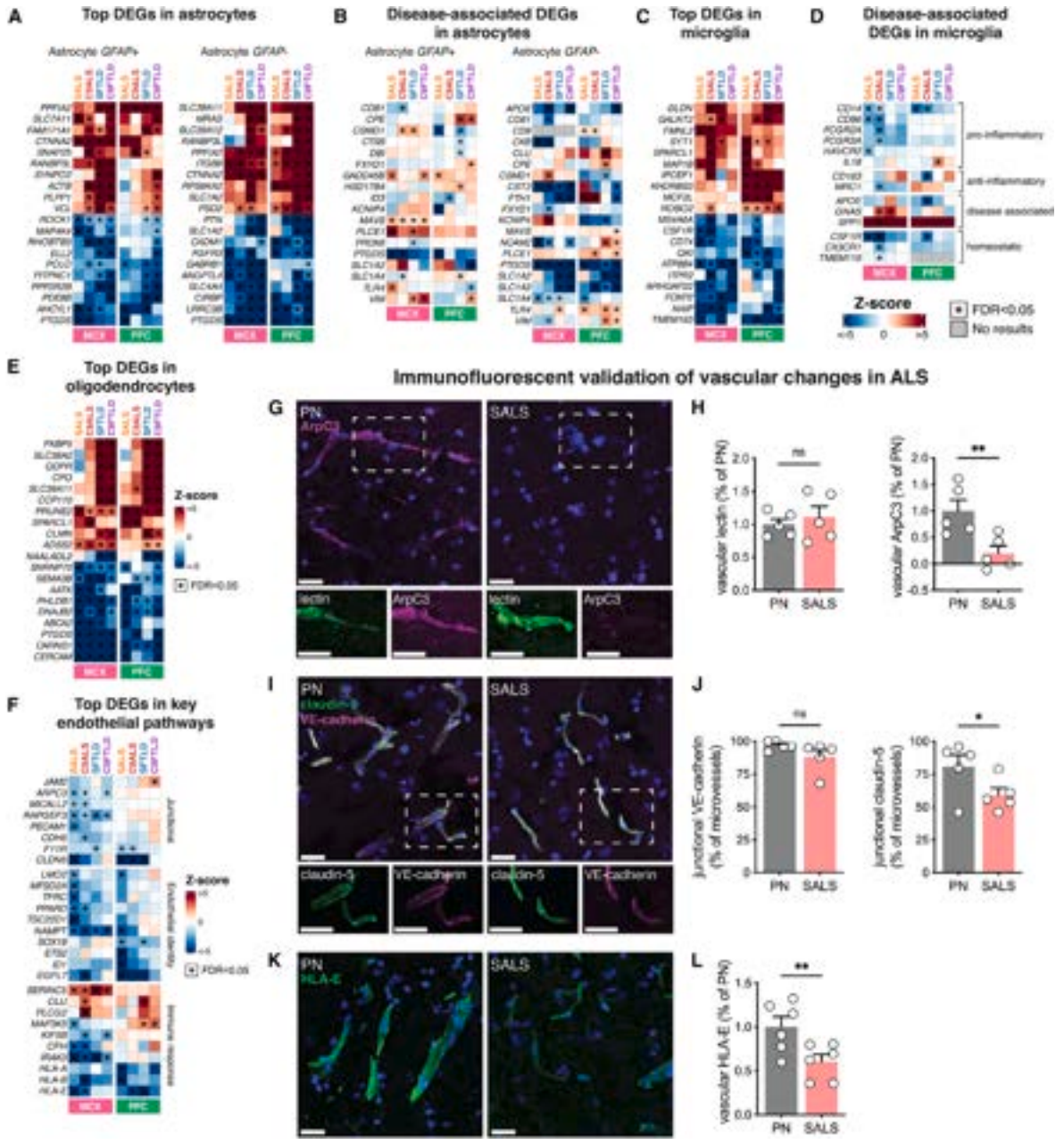

Figure 3. Non-neuronal disease mechanisms and vascular changes

(A) Top up- and downregulated genes shared across diseases in astrocyte populations.

(B) Differential expression of disease-associated astrocyte markers.

(C) Top up- and downregulated genes shared across diseases in microglia.

(D) Differential expression of microglial genes associated with disease response and homeostasis. Combined legend for (A)–(D).

(E) Top up- and downregulated genes shared across diseases in oligodendrocytes.

(F) Differential expression of select junctional, endothelial identity, and immune response genes in endothelial cells.

(G) Immunofluorescent labeling of ArpC3 with lectin in MCX. Lectin selectively labels blood vessels.

(H) Quantification of lectin and ArpC3 signal (n = 5 PN and n = 5 SALS donors).

(I) Immunofluorescent co-labeling of claudin-5 and VE-cadherin in MCX.

(legend continued on next page)

signatures recently observed in ALS spinal cord.[28,41,42] The upregulation of the activated glia markers observed was variable across phenotypes and brain regions (Figure 3B).

Supporting a shift to an activated microglia phenotype, we observed a downregulation of homeostatic microglia genes *CSF1R* and *CX3CR1* (Figures 3C and 3D). We observed some upregulation of a subset of disease-associated microglia markers previously seen in the spinal cord of an ALS mouse model and in the human ALS spinal cord,[28,43] including *GNAS*, *IL18*, and *SPP1* (Figure 3D). Additionally, we observed variable downregulation of inflammatory response pathway terms and other activated microglia markers such as *APOE*, *CD14*, *CD86*, and *HAVCR2* (Figures 3D and S2G).

In oligodendrocytes, we noted a dysregulation of genes encoding various metabolic factors, cell adhesion/ECM molecules, and proteostasis factors (Figure 3E). We further noted that oligodendrocytes displayed downregulation of genes involved in axon guidance (*SEMA3B*), myelination (*CNP*), as well as oligodendrocyte differentiation and specification (*SOX8*, *OLIG1*, and *OLIG2*). These suggest dysregulation of oligodendrocyte maturation and transcriptional identity with potential pathogenic consequences, especially for long-range projection neurons that would be dependent upon oligodendrocyte support for proper axonal function.[44–47] Negative enrichment of GO terms associated with oligodendrocyte development and differentiation was most pronounced in ALS (Figure S2H).

Vascular changes

Cerebrovascular dysfunction has been postulated to precede classical pathological changes and clinical symptoms in various neurodegenerative disorders.[48] Consistent with prior evidence of vascular leakage and tight junction loss,[49–53] we found that components of tight and adherens junctions were downregulated in MCX endothelial cells of ALS, and to a lesser extent FTLD cases, including *CLDN5*, *PECAM1*, *RAPGEF3*, and *MICALL2* (Figure 3F), but saw little evidence of the same in the PFC. We also observed reduced expression of brain endothelial-enriched transcription factors (*LMO2*, *PPARD*, and *TSC22D1*) and of transcripts associated with transcellular transport (*MFSD2A* and *TFRC*) and immune response (*IRAK3* and *HLA-E*), again in the ALS MCX (Figure 3F).

Downregulation of proteins encoding tight and adherens junction components would be expected to affect blood-brain barrier (BBB) integrity. Considering factors contributing to BBB dysfunction, we noticed that the ArpC3 subunit of the actin-related protein (Arp)2/3 complex (*ARPC3*) was downregulated pan-phenotypically in MCX endothelial cells (Figure 3F). Indirect immunofluorescence staining showed a stark depletion of vascular ArpC3 protein in the ALS MCX endothelium ($p = 0.003$) (Figures 3G and 3H). Because ArpC3 regulates the formation of tight and adherens junctions,[54,55] we hypothesized that endothelial junction proteins may also be mislocalized in ALS. To test this, we assessed the localization of tight junction protein claudin-5 (CLDN5) and adherens junction protein VE-cadherin (CDH5). Claudin-5 localization to junctions was diminished in ALS microvessels of the MCX ($p = 0.038$), as evidenced by a shift from strands of immunofluorescence toward cytoplasmic signal (Figures 3I and 3J). VE-cadherin co-localized with claudin-5 and seemed to also display diminished junctional localization but was not significant ($p = 0.077$). These data provide evidence of cerebrovascular dysfunction by reduced expression and mislocalization of tight junctions in the ALS motor endothelium and suggest a potential mechanism related to the loss of Arp2/3 complex machinery, similar to its effects in regulating tight junctions to promote epidermal barrier formation.[54]

Lastly, major histocompatibility complex (MHC) class 1 antigen E (*HLA-E*) emerged as a top endothelial DEG across ALS and FTLD (Figure 3F). HLA-E is an important regulator of natural killer (NK) cell function, specifically acting in endothelial cells as an inhibitory stimulus for NK-mediated cell lysis.[56,57] We observed reduced HLA-E protein expression in ALS MCX endothelial cells ($p = 0.010$) (Figures 3K and 3L). Previous work found elevated NK cells in serum, spinal cord, and MCX of ALS patients and SOD1 mouse models of ALS and reported that depletion of NK cells reduces motor neuron degeneration and increases survival.[58] Thus, loss of HLA-E from brain endothelium may represent a mechanism for NK-mediated BBB breakdown and/or NK cell parenchymal accumulation.

Drivers of cell-type-specific differential vulnerability

The L5 excitatory neurons linked to ALS and FTLD have been historically defined by morphology or projections, but their molecular identities have not been fully resolved. We integrated genetic information with our transcriptional data to pinpoint the transcriptional profiles of known and perhaps yet undiscovered differentially vulnerable cell types.

From the largest-to-date ALS genome-wide association study (GWAS),[59] we generated gene-level phenotype association statistics from identified single-nucleotide polymorphisms (SNPs) and used them to compute a per-cell susceptibility score based on SNP-linked gene enrichment (Figure 4A). This score represents a prediction of predisposition or "susceptibility" to differential vulnerability (measured by transcriptional dysregulation) based on known genetic factors. The results of this analysis show that L5 excitatory neuron populations scored the highest across brain regions (Figures 4A and 4B), signifying enrichment and co-expression of GWAS-linked genes and representing likely candidates for differential vulnerability. A differential enrichment analysis of the same gene set to identify SNP-linked genes enriched in each subtype showed a similar pattern with the *VAT1L+* (*Ex L5 VAT1L EYA4*) and *SCN4B+* (*Ex L3-5 SCN4B NEFH*) subtypes expressing the highest number of SNP-linked

(J) Quantification of junctional claudin-5 and VE-cadherin signals (n = 5 PN and n = 5 SALS donors).
(K) Immunofluorescent labeling of vascular HLA-E in MCX.
(L) Quantification of HLA-E signal (n = 6 PN and n = 6 SALS donors).
In (G), (I), and (K), the scale bars, 50 μm. In (H), (J), and (L), the error bars represent the standard error of the mean. (*) $p < 0.05$; (**) $p < 0.01$; unpaired one-tailed t test.
See Figure S2.

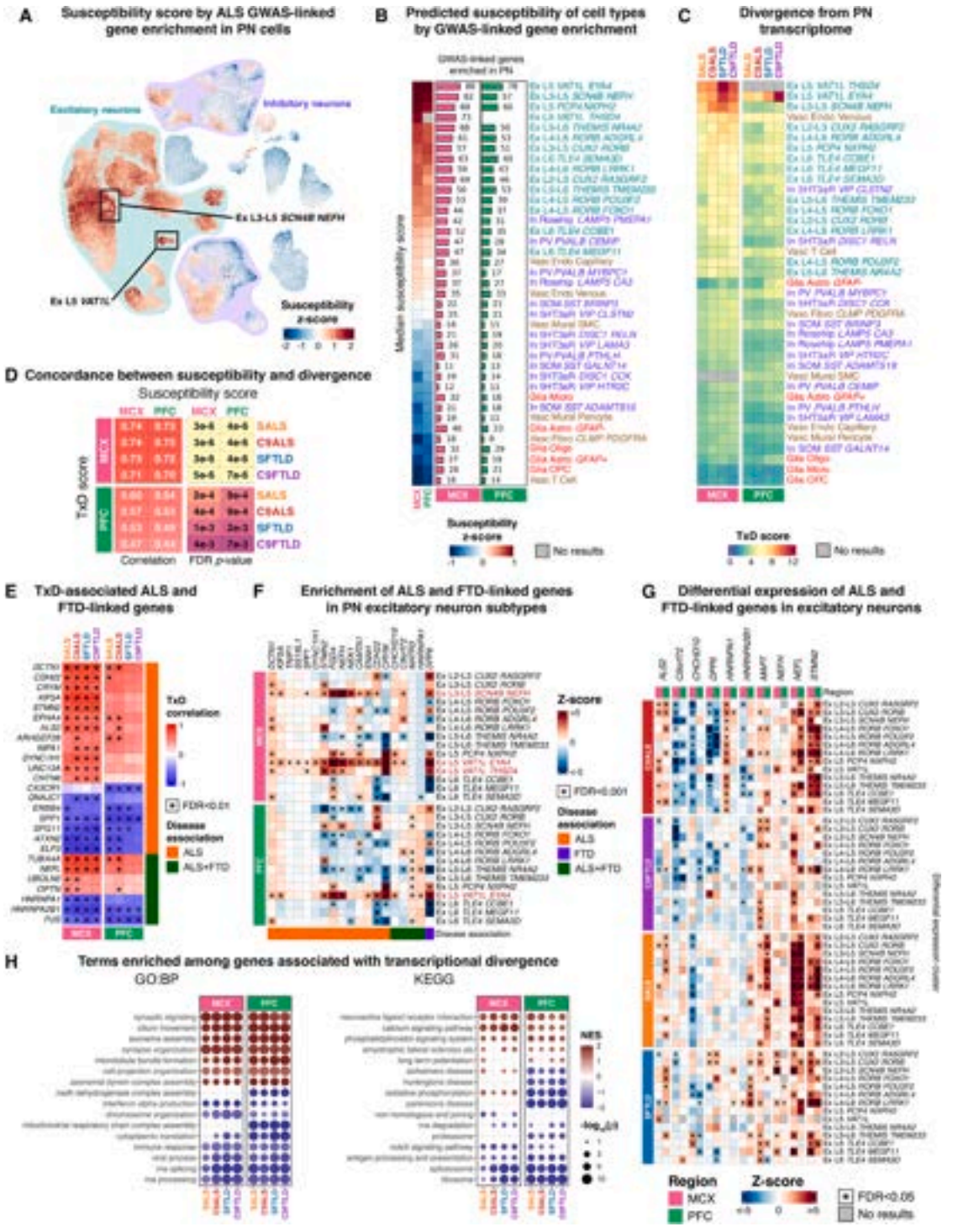

(legend on next page)

genes (Figure 4B). Unfortunately, the lack of a well-powered GWAS precluded this analysis for FT(L)D.

The susceptibility analyses are based on endogenous gene expression in PN post-mortem tissue with the intent of predicting disease response. With cell-type-specific gene expression data in hand, we could directly quantify that response across our cohort. For each subtype, we computed a transcriptional divergence score (TxD score), which quantifies the magnitude of transcriptional dysregulation (Figure 4C; STAR Methods). This analysis revealed that *VAT1L*+ (both subtypes) and *SCN4B*+ excitatory subtypes were dramatically more dysregulated than all other cell types across disease groups. *VAT1L*+ neurons likely comprise or contain the UMN, and spindle populations known to be depleted in ALS and FTLD, but the significance of the *SCN4B*-expressing population is unknown. This subtype shows greater than expected similarity to the *VAT1L*+ neurons (Figure 1F) but is more closely related to the less vulnerable translaminar neurons with which it clusters. Remarkably, this analysis also shows a region-dependent differential disease response. The *SCN4B*+ MCX population is almost as dysregulated as the putative UMN clusters, whereas its PFC counterpart is no more dysregulated on average than any other translaminar excitatory subtype (Figure 4C). Overall, these measurements mirror those obtained from the GWAS gene enrichment analysis. We compared the GWAS-predicted susceptibility scores with the observed TxD scores and found that they are strikingly well correlated (Figure 4D). This implies that population-level genetics are strongly predictive of cell-type-specific differential vulnerability.

Next, we examined the relationship between expression of known disease-linked genes and transcriptional dysregulation. This "TxD-association analysis" identified genes that may represent either molecular risk factors or those whose expression might serve as a predictor of susceptibility. We looked at 65 genes expressed in our data whose association with ALS or FTD is supported by the literature and found 16 to be positively correlated with TxD (FDR < 0.01) (Figures 4E and S3A). Six of these genes (*DCTN1*, *TUBA4A*, *NEFL*, *KIF5A*, *STMN2*, and *DYNC1H1*) are linked to axonal structure or transport. The interpretation of strongly negatively correlated genes is more ambiguous because this could suggest a protective role of these genes in disease or that said gene is absent in vulnerable cell types.

The observation that disease-linked gene expression is correlated with dysregulation led us to identify three cell types enriched for these genes (Figure 4F). L5 *VAT1L*+ neurons exhibited the highest enrichment, in particular the regionally conserved *EYA4*+ subtype (*Ex L5 VAT1L EYA4*), and more so in the MCX. Surprisingly, the L3/5 *SCN4B*+ cell type in the MCX was enriched for a dozen disease-linked genes, implying that this cell type warrants further investigation for association with ALS/FTLD pathology. We also looked for enrichment of genes associated with other axonal disorders (spinal muscular atrophy [SMA], Charcot-Marie-Tooth disease [CMT]), as well as other common neurodegenerative diseases (Alzheimer's [AD], Parkinson's disease [PD]). We did not observe enrichment of known AD, PD, or SMA-linked genes beyond those already linked to ALS or FTD, but saw marginal enrichment of CMT-linked genes (data not shown).

We next assessed how ALS- and FTD-linked gene expression was altered in disease. We identified a handful of genes with notable disease-associated expression patterns (Figure 4G). As established by the pan-neuronal DEG analysis (Figure 2D), *STMN2* and *NEFL* are among the most upregulated genes showing no cell-type-specific expression pattern. Upregulation of these, along with *MAPT*, may reflect a compensatory response to axonal damage.[60,61] Downregulation of *C9orf72* in the blood and spinal cord of G_4C_2 expansion carriers has been previously reported.[28,62] We report that this downregulation is not cell-type specific in the human cortex, with *C9orf72* being among the most downregulated genes across most cell types in our data but only in C9 cases. Notably, this downregulation appears broader in the MCX. In ALS, neurofilament heavy chain (*NEFH*), bound by SMI-32 and sometimes used as a marker of UMNs, was selectively upregulated in the UMN-like L5 *VAT1L*+ neurons of the MCX. Other genes, such as the ALS-causative gene *HNRNPA1*, showed a disease-specific dysregulation pattern restricted to C9ALS MCX.

We repeated the TxD-association analysis across the entire transcriptome to identify new genes whose expression may be strongly correlated with dysregulation. One might expect that top-ranking genes would include marker genes of vulnerable cell types, but this was not the case. Among the top-ranking TxD-associated genes in both brain regions was *LYNX1* (Figure S3B). LYNX1 interacts with nicotinic acetylcholine receptors (nAChRs) and is thought to modulate their activity, preventing excessive excitation.[63,64] Given that smoking is the only widely

Figure 4. Drivers of cell-type-specific differential vulnerability

(A) Heatmap of disease susceptibility scores based on ALS GWAS-linked gene enrichment. Scores superimposed on PN cells of UMAP from Figure 1A.

(B) Heatmap on the left shows the median susceptibility scores per subtype. Bar plot on the right shows the number of GWAS-linked genes enriched in each subtype. Wilcoxon rank sum test (log_2-fold change Z score > 1 and FDR < 0.001).

(C) Transcriptional divergence (TxD) score of subtypes by disease and brain region.

(D) Left: Pearson correlation between susceptibility (from B) and TxD (from C) scores. Right: FDR-adjusted correlation p values of corresponding comparisons on the left.

(E) TxD association analysis of ALS- and FTD-linked genes. Genes with a significant association with more than one disease group are shown. See extended Figure S3A for all genes.

(F) Differential enrichment of ALS- and FTD-linked genes across excitatory neuron subtypes. Differentially vulnerable (by TxD score) subtypes are denoted in red. Genes enriched in at least one vulnerable subtype are shown.

(G) Differential expression of select ALS- and FTD-linked genes across excitatory neurons in disease.

(H) Select top-ranking GO terms (left) and KEGG pathways (right) enriched among TxD-associated genes. Terms have a positive normalized enrichment score (NES) if enriched among positively correlated genes and negative otherwise.

See Figure S3.

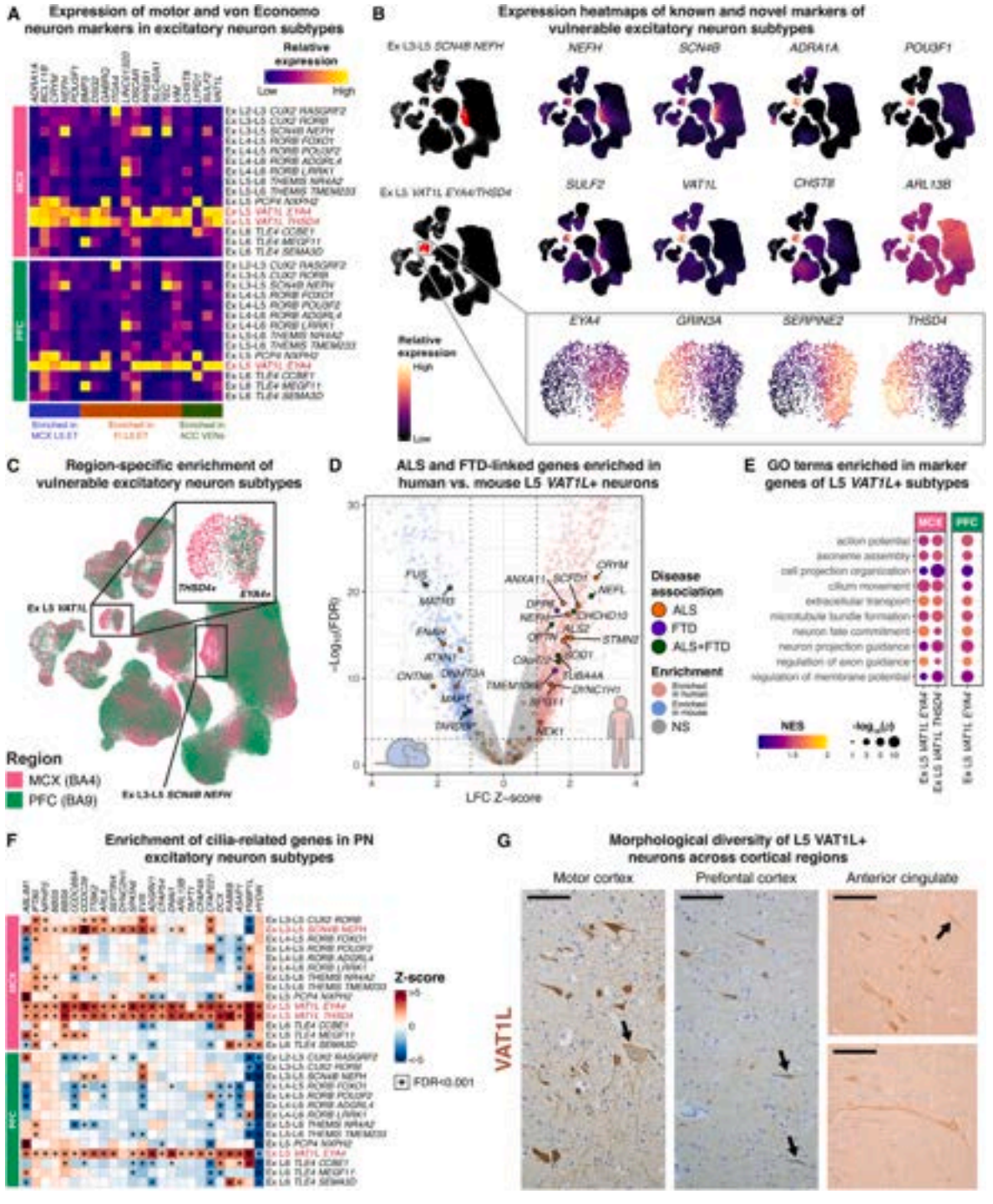

(legend on next page)

accepted environmental risk factor for ALS,[65] it is possible that nicotine exposure from smoking results in hyperexcitation of L5 neuron nAChR activity, normally counteracted by LYNX1.

GSEA identified many positively TxD-associated GO terms related to primary ciliary function, organization, and assembly across disease groups (Figures 4H and S3C). Primary cilia are believed to play a role in axonal guidance,[66] which may relate to enhanced vulnerability of long-range projection neurons highly dependent on this process. Many terms and genes associated with axon development and repair were found to be positively associated (Figure S3C), which is expected given that long-range projection neurons are the most affected cell types. Terms enriched among negatively correlated genes centered around RNA metabolism, the ribosome, and anti-viral immunity (Figures 4H and S3C). The association of mitochondrial metabolism and OXPHOS-related genes appeared to be highly region specific (Figure S3C). Among the Kyoto Encyclopedia of Gene and Genomes (KEGG)[67] terms, there was a region-dependent enrichment of neurodegeneration terms, including ALS and dementias (Figure 4H).

Finally, a stark number of the most positively correlated genes were not only enriched across vulnerable populations but also broadly dysregulated with region, phenotype, or genotype specificity (Figure S3D). Among these was *TBR1*, which is normally expressed at high levels in L6 neurons and at low levels in L5b neurons according to our data and prior reports[68] and is known to repress *FEZF2* transcription and thus repress its activity in subplate L6 corticothalamic projection neurons in order to restrict the corticospinal tract origin to L5.[69]

Characterization of vulnerable L5 excitatory populations

Having identified differentially vulnerable transcriptional signatures, we aimed to characterize these clusters in greater detail. In ALS, the vulnerability of MCX-specific L5 ET projection neurons, generally believed to be UMNs, is well established. Best known are the giant Betz cells that synapse directly onto the LMNs. Similarly, the loss of L5 frontally enriched, spindle-like VENs and fork cells has been linked to behavioral-variant FTD[17,70] and is considered a pathological hallmark of several FTD subtypes, including FTLD-TDP.[71] Despite the molecular and pathological similarities between ALS and FTLD, among non-comorbid cases, these diseases initially exhibit non-overlapping affected region and cell-type-specific progression patterns, and their most selectively vulnerable populations are not known to coexist.

To identify these canonically implicated cells, we looked at the expression of known UMN, VEN, and L5 ET projection neuron markers in the relevant brain regions (Figure 5A).[21,25,72–74] L5 *VAT1L*+ neurons, which partitioned into two subclusters, *EYA4*+ and *THSD4*+ (the latter detected almost exclusively in the MCX), selectively expressed nearly all reported marker genes (Figures 5A and 5B). UMNs and spindle neurons share few morphological similarities and have no known overlap in their localization or projections other than both residing in L5. It was remarkable to see that markers of both overlapped perfectly onto the same cluster (Figure 5B), indicating near indistinguishable transcriptional profiles. We chose to use the marker gene *VAT1L* to identify this cell population given its global specificity (Figures 5B and S4A). We also identified *ARL13B*, a ubiquitously expressed gene greatly enriched in L5 *VAT1L*+ neurons, as a potential marker of this population (Figures 5B and S4A). ARL13B regulates Sonic hedgehog signaling and is involved in the maintenance of the ciliary axoneme structure.[75,76] More importantly, *ARL13B* is a canonical marker of primary cilia, whose constituent pathway gene expression is both dysregulated in disease (Figures 2C, 6D, and 6E) and strongly correlated with susceptibility and transcriptional divergence (Figures 4H and S3C).

The L5 *VAT1L*+ cluster was enriched for long-range projection and large axon caliber markers *NEFH* and *SCN4B* (Figure 5B), but as mentioned, L3/5 *SCN4B*+ neurons (*Ex L3-L5 SCN4B NEFH*) expressed these at even higher levels. Strikingly, these neurons also appear to be differentially vulnerable in disease (Figure 4C), are the next most transcriptionally similar to L5 *VAT1L*+ neurons (Figure 1F), and are enriched for ALS- and FTD-associated genes (Figure 4F). Furthermore, these two cell populations are the only excitatory cell types that showed clear regional heterogeneity in their distribution, with both possessing an MCX-enriched subpopulation (Figure 5C).

The significance of ALS- and FTD-linked gene expression in vulnerable cell types has come under renewed interest following reports of human-specific enrichment of these genes in spinal LMNs.[77] Having established that these genes are highly enriched in cortical UMNs (Figure 4F), we sought to determine if this enrichment was also human specific. We performed snRNA-seq of mouse MCX from 8-week-old C57BL/6J mice and recovered a transcriptional landscape resembling that of the human MCX (Figure S5A). Corticospinal motor neurons (CSMNs) are well conserved across mammals and have been thoroughly

Figure 5. Characterization of vulnerable L5 excitatory populations

(A) Relative expression of known markers of L5 ET neurons, including those with Betz and VEN morphology, from various brain regions.

(B) Heatmaps superimposed on Figure 1B showing relative expression of known and novel markers of differentially vulnerable excitatory neuron subtypes (whose location in the UMAP is shown on the left). Inset shows markers that distinguish subtypes of L5 *VAT1L*+ neurons.

(C) UMAP of excitatory neurons (same as Figure 1B) colored by brain region of origin. Inset: region-specific heterogeneity of L5 *VAT1L*+ subtypes.

(D) Differential expression of ALS and FTD-linked genes in L5 *VAT1L*+ neurons between human and mouse MCX. Only statistically significant (Z score > 1 and FDR < 0.001) genes are marked. NS: not significant.

(E) Select top-ranking GO terms enriched in marker genes of human L5 *VAT1L*+ subtypes. See Figure S4B for extended results.

(F) Differential enrichment of cilia-associated genes across excitatory neuron subtypes. Differentially vulnerable subtypes are denoted in red. See Figure S4C for extended results.

(G) Representative images of IHC labeling of VAT1L (brown) in PN MCX (left), PFC (middle), and ACC (right). Black arrows denote cells with Betz (in MCX) or spindle (in PFC and ACC) morphology. Scale bars, 100 μm.

See Figures S4 and S5.

characterized in mice,[72,73] leading to the identification of CSMN markers such as *Crim1*, *Diaph3*, and *Igfbp4*. We identified a single *Vat1l*-expressing cluster that closely matched human L5 *VAT1L*+ neurons (Figure S5B) and expressed these canonical mouse CSMN markers (Figure S5C). This population selectively expressed many of the same human (and mouse) L5 ET markers (Figure S5D) but did not partition into subclusters based on the identified L5 *VAT1L*+ MCX subtype markers (Figure S5E). Differential expression analysis between human and mouse L5 *VAT1L*+ neurons identified 17 statistically significant (Z score > 1 and FDR < 0.001) ALS- and FTD-associated genes enriched in human cells (Figure 5D). This includes all ALS genes enriched in human LMNs (*NEFH*, *NEFL*, *SOD1*, *TUBA4A*, and *CHCHD10*),[77] except for *SPP1*, which was statistically significant but subthreshold in magnitude.

Pathway enrichment analysis of L5 *VAT1L*+ neuron marker genes (Figures 5E and S4B) identified expected terms related to axon structure and maintenance, but more surprisingly, cilia-associated terms such as ciliary movement and axoneme assembly also emerged, supporting a role for this organelle in disease susceptibility. We further identified almost 50 cilia-associated genes that were highly enriched across L5 *VAT1L*+ and L3/5 *SCN4B*+ neurons (Figure S4C). Although many cilia genes are also microtubule associated and therefore expected to be enriched in long-range projection neurons, we found that roughly half were cilium specific (Figure 5F).

Betz cells comprise a relatively rare cortical population, accounting for 10%–15% of MCX L5b.[22] Although Betz cells are just one type of UMN, other MCX-residing subtypes are not morphologically distinct and have not been specifically quantified. Spindle neurons are rarer, making up only 3% of ACC L5, where they are most abundant and less abundant in other brain regions.[18,23] In either case, these bounds mean that they should comprise far less than the total proportion of L5 *VAT1L*+ neurons present in our data. We quantified the morphological diversity of cells in this cluster across cortical regions by immunohistochemical (IHC) staining of VAT1L.

First, we confirmed that VAT1L labels UMNs, specifically Betz cells and spindle neurons in their respective cortices, and only labels neurons in L5, as the transcriptomic data indicated (Figures 5A, 5B, and S4A). We found that disease-implicated morphologies made up a minority of the VAT1L+ cells (Figure 5G). In the MCX, we observed ~11% of VAT1L+ cells to have stereotypical Betz morphology (data not shown). Betz cells are identified by their size and laminar distribution, their large nucleus, and conspicuous nucleolus.[22] We noticed that they also have a distinct VAT1L somatic staining pattern (Figure 5G). Prior reports place spindle neuron abundance at less than 1% of BA9 L5, with a very different distribution, usually being found in isolation or in pairs.[18] VAT1L staining of PFC recapitulated this observation, labeling sparse bipolar neurons in L5 and otherwise unremarkable pyramidal neurons in the same location just as in the MCX (Figure 5G). As predicted by the single-cell data, VAT1L+ cells were less abundant in the PFC (Figure S4D). As a secondary validation, we performed immunofluorescent labeling of pan-neuronal cell-filling marker NeuN, and the nuclear-localized transcription factor POU3F1, which shows an almost identical RNA expression profile as VAT1L (Figures 5A, 5B, and S4A). In MCX L5, we observed identical results to the VAT1L stain, observing both Betz and non-Betz POU3F1+ cells (Figure S4E), but we did not observe any POU3F1- neurons with Betz morphology.

Having transcriptionally identified differentially vulnerable cell types and shown that they encompass morphologies implicated in ALS and FTLD, we then investigated the VAT1L+ cells that do not possess clear Betz or spindle morphology because these make up the overwhelming majority of L5 VAT1L+ neurons. It is unlikely that the extreme dysregulation observed in L5 *VAT1L*+ cells is driven by the small subset of neurons with disease-linked morphology, especially because they all appear to share the same transcriptome. Furthermore, a similar transcriptional profile has been previously identified in FI snRNA-seq data and shown to encapsulate stereotypical VENs.[21] We thus have reason to believe that this identity may be conserved across cortical regions and extend to vulnerable L5 cells in other regions, such as the ACC. VAT1L has been proposed as an ACC VEN marker,[74,] and indeed, IHC labeling of VAT1L in the ACC of the same patients confirms a histological profile similar to PFC, including the presence of canonical VENs (Figure 5G). This is significant because prior studies reported the GABA receptor subunit, GABRQ, as a marker of differentially vulnerable cells in the ACC of FTD cases and showed that VENs were a subset of a larger population of predominantly pyramidal L5 GABRQ+ neurons, which were largely depleted.[78,79] In our data, *GABRQ* is expressed in the same cluster as *VAT1L* (Figure 5A), indicating that this ACC population might represent the same vulnerable and transcriptionally synonymous cells present in the MCX, PFC, and FI. This implies that non-Betz and non-spindle VAT1L+ neurons in the MCX, PFC, and perhaps other brain regions might be differentially vulnerable, independent of priorly known morphologically defined subtypes.

Impact of disease on differentially vulnerable cell types

To answer the question of whether all L5 *VAT1L*+ neurons from these brain regions are differentially vulnerable in ALS and/or FTLD, or if Betz and spindle cells are solely driving the apparent dysregulation and the likely depletion of this cluster, we performed a series of histological analyses of VAT1L+ neurons. We first confirmed TDP-43 pathology in the candidate neurons (Figure 6A). We then performed histological quantification of L5 VAT1L+ cells in ALS and FTLD to determine if the observed dysregulation was consistent with neuronal loss (Figures 6B, 6C, S6A, and S6B). In the MCX, we observed a 30% reduction ($p = 0.003$) of VAT1L+ cells in ALS, but not in FTLD ($p = 0.186$) (Figures 6B, S6A, and S6B), despite substantial dysregulation in the latter (Figure 4C). Conversely, we saw a 26.5% reduction ($p = 0.02$) of VAT1L+ cells in the PFC of FTLD donors, but not in ALS ($p = 0.279$). Next, we assessed if this loss was driven by canonically implicated morphological subtypes or if it was across all VAT1L+ cells. With this having been previously confirmed in FTLD, albeit in a different brain region, we focused on ALS MCX and repeated this analysis with genotype resolution, distinguishing between Betz and non-Betz pyramidal cells. We observed, among both sporadic and C9 ALS cases, a severe loss of VAT1L+ cells with Betz morphology, but more remarkably, we also observed the loss

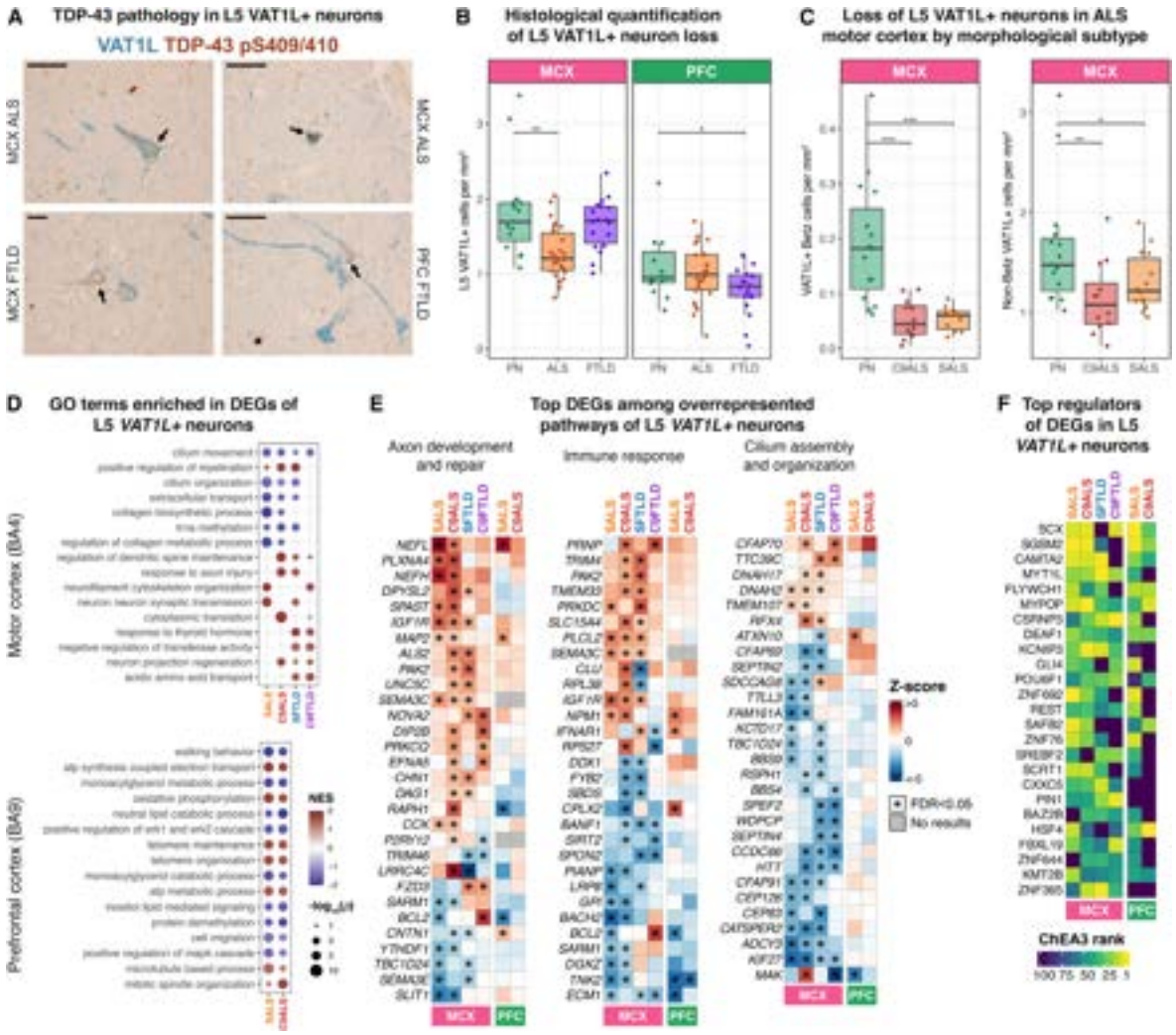

Figure 6. Impact of disease on differentially vulnerable cell types

(A) Representative images of VAT1L and TDP-43 pS409/410 in diseased tissue samples by IHC. Black arrows denote intraneuronal inclusions. Scale bars, 50 μm.

(B and C) Histological quantification of VAT1L+ neuron density in L5 across brain regions and diseases. In (B), all L5 VAT1L+ neurons are quantified. In (C), only neurons with Betz (left) or non-Betz (right) morphology are considered. Box and whisker plots show median and interquartile range values. (*) $p < 0.05$; (**) $p < 0.01$; (***) $p < 0.001$; one-tailed t test.

See Figure S6A for a table of results.

(D) Enrichment of top-ranking GO terms in DEGs of L5 *VAT1L*+ neurons by brain region.

(E) Top DEGs of overrepresented GO term families enriched in L5 *VAT1L*+ neurons.

(F) Top-ranking ChEA3-predicted regulators of L5 *VAT1L*+ neurons DEGs. Values are the mean rank across ChEA3 libraries.

See Figure S6.

of non-Betz VAT1L+ neurons (C9ALS: −30.6%, p = 6.8e−3; SALS: −20.3%, p = 0.035) (Figures 6C, S6A, and S6B). However, cells with Betz morphology were substantially more depleted (C9ALS: −72.2%, p = 1.4e−4; SALS: −71.5%, p = 1.5e−4). These data support the hypothesis that differential vulnerability in ALS and FTLD transcends traditional morphologically implicated cell types and that all cells sharing this molecular identity are susceptible to enhanced dysregulation and cell death.

Having confirmed the disease relevance of L5 *VAT1L*+ neurons in both ALS and FTLD, we focused on transcriptional alterations in this population. For cell-type-specific DEG analysis, we treated *VAT1L*+ cells as a single group due to the rarity of individual subtypes. This analysis was further limited by the lack of sufficient cells in the PFC of FTLD cases. Because these were terminal cases, this already rare population was too depleted to perform a rigorous analysis.

We observed changes to expected ALS-linked mechanisms (e.g., axon development and repair, RNA processing, OXPHOS, and nucleocytoplasmic transport) (Figures 6D and 6E),[80,81] as well as DEGs and pathways related to innate immune signaling, consistent with reports of double-stranded RNA accumulation and innate immune activation in ALS and FTLD (Figure 6E).[82,83] In addition, we also noted several primary cilium-related genes and terms, including cilium organization, cilium movement, and motile cilium assembly (Figures 6D and 6E). Although downregulation of these was observed in the pan-excitatory analysis, these terms and genes are enriched in L5 *VAT1L+* cells under normal conditions, suggesting that they may be more dependent on these genes and making their loss more damaging.

Ciliary-basal-body- and ciliopathy-linked gene *BBS4* was among the significantly downregulated genes in C9 cases (Figure 6E). *BBS4* interacts with ALS-linked gene *DCTN1*,[84] which is one of the most strongly TxD-associated genes (Figure 4E) and is enriched in L5 *VAT1L+* neurons (Figure 4F). A causal link between these primary cilium genes and ALS and FTLD is established by the identification of ciliopathy disease gene cilia- and flagella-associated protein 410 (*CFAP410/C21orf2*) as an ALS risk gene.[85,86]

Top ChEA3-predicted[87] DEG regulators in L5 *VAT1L+* cells included MYT1L and REST (Figure 6F), confirming a broad dysregulation of terms related to neuronal function and identity.[88,89] Another top regulator, SREBF2, is a master regulator of cholesterol biosynthesis[90] and has been shown to be dysregulated by altered TDP-43 levels.[91]

We also briefly highlight results from the potentially ALS- and/or FTLD-relevant L3/5 *SCN4B+* neurons. Just as L5 *VAT1L+* and L3/5 *SCN4B+* neurons share molecular characteristics and appear to be similarly dysregulated in the MCX, we found that the disease-associated transcriptional changes are also similar. Across ALS, these two subtypes showed the highest similarity in their dysregulation patterns in terms of individual genes, enriched pathways, and predicted regulators relative to other groups (Figures S6C–S6E), highlighting a potentially important role for these neurons in ALS.

DISCUSSION

Our data demonstrate that cell-type-specific components of disease-induced gene dysregulation are conserved across ALS and FTLD and that there is an unequivocally high similarity of sporadic versus familial (C9) ALS/FTLD-induced gene expression changes. This suggests that the mechanisms of *C9orf72* G_4C_2-mediated toxicity likely precede most disease-associated transcriptional alterations because downstream molecular and pathological changes are largely indistinguishable between sporadic and C9 cases, although we identified a few divergent pathways. ALS-linked protein, NEFL, is a robust biomarker of axonal degeneration and was greatly upregulated in ALS without cell-type specificity. This broad and potentially compensatory response to axonal degradation might explain why NEFL is found at high levels in the blood and CSF of ALS patients. In addition, we observed impairment of cerebrovascular integrity and homeostasis indicated by loss of tight and adherens junction genes and key regulators thereof and regulators of NK cell activity.

We identified differentially vulnerable cell populations and demonstrated the convergence of population-level genetic risk factors and transcriptional dysregulation using an approach that could be extended to other disorders where differentially vulnerable cell types are ill-defined or unknown. Among these highly affected populations, we recovered motor and spindle neuron populations and conclusively showed that they possess almost indistinguishable transcriptional identities. The most striking feature of this putative vulnerability signature is the enrichment and co-expression of numerous ALS- and FTLD-linked genes, which overlap with those reported to be preferentially expressed in spinal cord LMNs. Other genes overrepresented in this risk fingerprint include primary cilia and axoneme-related genes, some of which have been previously linked to ALS and numerous ciliopathies. Human ciliopathy disorders are characterized by developmental axonal malformations and axonal pathfinding abnormalities,[92,93] and it is known that primary cilium-related genes have important developmental axonal functions. The enrichment of these genes in the most vulnerable cell types suggests an unexplored determinant of cell-type-enhanced vulnerability. We also identify a likely susceptible and highly dysregulated L3/5 *SCN4B+* excitatory neuron population in the MCX that shares many of these disease-relevant molecular characteristics with UMNs and spindle neurons.

We demonstrate that UMNs and spindle neurons in the MCX and PFC both belong to a larger population of L5 VAT1L+ neurons that is vulnerable and depleted in ALS and FTLD with region-phenotype specificity, expanding the scope of ALS- and FTLD-implicated cell types and potential therapeutic targets. Using stereological approaches, we find that there is further granularity in susceptibility that can be broken down into morphological subtypes, with Betz cells exhibiting more extensive loss than their transcriptionally identical, non-Betz counterparts. This finding, along with previous reports in the ACC, makes a compelling argument for using molecular identity as a criterion for classifying vulnerable cell types in ALS and FTLD. This, along with the conserved risk factors identified between UMNs and LMNs, establishes a transcriptional link between distinct susceptible populations across the nervous system and the ALS-FTLD pathological spectrum.

Limitations of the study

Although the methods here have enabled the investigation of cell-type-specific disease mechanisms, key limitations of the snRNA-seq assay leave the opportunity for future studies and improvements. Of recent interest to the field is the role of microglia in disease pathogenesis; yet, our data only partially reflect microglial changes, given that nuclear profiling has been found to have limited capability in detecting changes to microglial activation genes in tissue.[94] Another limitation of the assay and use of human tissues is the expected variability in dissections and nuclei capture resulting in highly variable cell-type yields even from high-quality and rigorously dissected tissues, making it a poor method for evaluating changes in cell-type composition. This mandates the use of histology, or similar

approaches, to validate such changes, similar to those in L5 VAT1L+ neurons. However, it may not be feasible to scale this to many populations. The current limited understanding of FTD genetics, relative to ALS, restricts our ability to present a well-balanced analysis of the two diseases in many cases. A well-powered FT(L)D GWAS would help bridge the gap in understanding the genetic landscape of the ALS-FTD disease spectrum and enable the discovery of cell-type-specific genetic drivers of pathology. Lastly, low cell yields make studying very rare populations difficult, which, in this case, prevented us from studying changes to L5 *VAT1L*+ neurons in FTLD PFC. Future studies could tackle this using targeted cell-type recovery methods.

STAR★METHODS

Detailed methods are provided in the online version of this paper and include the following:

- KEY RESOURCES TABLE
- RESOURCE AVAILABILITY
  - Lead contact
  - Materials availability
  - Data and code availability
- EXPERIMENTAL MODEL AND SUBJECT DETAILS
  - Data reporting
  - Human samples
  - Animals
- METHOD DETAILS
  - Human sample preparation
  - Mouse sample preparation
  - Isolation of nuclei from post-mortem fresh frozen human and fresh mouse brain tissue
  - Library preparation and sequencing
  - Sequencing data preprocessing
  - Immunofluorescent labeling and confocal microscopy
  - Immunofluorescent image quantification
  - Immunohistochemistry and stereology
- QUANTIFICATION AND STATISTICAL ANALYSIS
  - Cell clustering and curation
  - Cell type annotation
  - Alternative annotations
  - Differential gene expression analysis
  - Pathway enrichment analysis
  - Predicting upstream regulators
  - Cross-region and cross-species comparisons
  - Preprocessing pseudo-bulk expression for multiple analyses
  - Calculation of transcriptional divergence scores
  - Scoring TxD association
  - SNP-to-gene mapping and gene level GWAS statistics
  - Disease susceptibility scoring
  - Differential enrichment analyses

SUPPLEMENTAL INFORMATION

Supplemental information can be found online at https://doi.org/10.1016/j.cell.2024.02.031.

ACKNOWLEDGMENTS

The work was supported by funding from the National Institutes of Health (R01 NS127187 to M.H., V.V.B., and M.K., R35 NS127327 to M.H., U01 NS110453 to M.K., R01 AG067151 to M.K. and V.V.B., T32 EB019940 to S.S.P., and F32 NS128067 to R.M.L.), Mitsubishi Tanabe Pharma Holdings America, Inc., the JPB Foundation, the Robert Packard Center for ALS Research at Johns Hopkins, the LiveLikeLou Foundation, the Gerstner Family Foundation, the Mayo Clinic Center for Individualized Medicine, and the Cure Alzheimer's Fund. H.L. and B.E.F. were supported by fellowships from the JPB Foundation. We acknowledge the expertise and assistance of Marka Van Blitterswijk, Julio Mantero, Cyril Pottier, Rosa Rademakers, Jaimin Shah, Ronald Petersen, Neill Graff-Radford, Bradley Boeve, David Knopman, Keith Josephs, Sami Barmada, Mariely DeJesus-Hernandez, Raquel Morales-Gallel, Jose Manuel Garcia-Verdugo, Anna Shcherbina, and Makoto Tamura. The authors want to thank the patients and their families for their generous brain donations.

AUTHOR CONTRIBUTIONS

S.S.P., H.L., and K.G. performed transcriptional profiling. S.S.P. performed computational analyses. R.M.L. performed vascular validation, and S.S.P. and B.E.F. performed all other immunofluorescence validation. M.J.U.-N., E.E.-C., and M.C.C. performed IHC and stereology. F.J.G. performed mouse experiments. V.V.B., D.W.D., M.E.M., L.J.P., M.E.G., M.D., D.V.V.-G., A.T.S.H., and B.E.O. provided biological samples and pathological information. M.H., M.K., and V.V.B. jointly supervised the work. S.S.P., M.H., and R.M.L. wrote the manuscript.

DECLARATION OF INTERESTS

The authors declare no competing interests.

Received: February 16, 2023
Revised: November 9, 2023
Accepted: February 23, 2024
Published: March 22, 2024

REFERENCES

1. Couratier, P., Corcia, P., Lautrette, G., Nicol, M., and Marin, B. (2017). ALS and frontotemporal dementia belong to a common disease spectrum. Rev. Neurol. (Paris) *173*, 273–279.
2. Burrell, J.R., Kiernan, M.C., Vucic, S., and Hodges, J.R. (2011). Motor Neuron dysfunction in frontotemporal dementia. Brain *134*, 2582–2594.
3. Giordana, M.T., Ferrero, P., Grifoni, S., Pellerino, A., Naldi, A., and Montuschi, A. (2011). Dementia and cognitive impairment in amyotrophic lateral sclerosis: a review. Neurol. Sci. *32*, 9–16.
4. Gordon, P.H., Delgadillo, D., Piquard, A., Bruneteau, G., Pradat, P.F., Salachas, F., Payan, C., Meininger, V., and Lacomblez, L. (2011). The range and clinical impact of cognitive impairment in French patients with ALS: A cross-sectional study of neuropsychological test performance. Amyotroph. Lateral Scler. *12*, 372–378.
5. Lomen-Hoerth, C., Anderson, T., and Miller, B. (2002). The overlap of amyotrophic lateral sclerosis and frontotemporal dementia. Neurology *59*, 1077–1079.
6. Ringholz, G.M., Appel, S.H., Bradshaw, M., Cooke, N.A., Mosnik, D.M., and Schulz, P.E. (2005). Prevalence and patterns of cognitive impairment in sporadic ALS. Neurology *65*, 586–590.
7. Neumann, M., Sampathu, D.M., Kwong, L.K., Truax, A.C., Micsenyi, M.C., Chou, T.T., Bruce, J., Schuck, T., Grossman, M., Clark, C.M., et al. (2006). Ubiquitinated TDP-43 in frontotemporal lobar degeneration and amyotrophic lateral sclerosis. Science *314*, 130–133.
8. Ling, S.-C., Polymenidou, M., and Cleveland, D.W. (2013). Converging mechanisms in ALS and FTD: disrupted RNA and protein homeostasis. Neuron *79*, 416–438.

9. DeJesus-Hernandez, M., Mackenzie, I.R., Boeve, B.F., Boxer, A.L., Baker, M., Rutherford, N.J., Nicholson, A.M., Finch, N.A., Flynn, H., Adamson, J., et al. (2011). Expanded GGGGCC hexanucleotide repeat in noncoding region of C9ORF72 causes chromosome 9p-linked FTD and ALS. Neuron *72*, 245–256.

10. Renton, A.E., Majounie, E., Waite, A., Simón-Sánchez, J., Rollinson, S., Gibbs, J.R., Schymick, J.C., Laaksovirta, H., van Swieten, J.C., Myllykangas, L., et al. (2011). A hexanucleotide repeat expansion in C9ORF72 is the cause of chromosome 9p21-linked ALS-FTD. Neuron *72*, 257–268.

11. Abramzon, Y.A., Fratta, P., Traynor, B.J., and Chia, R. (2020). The Overlapping Genetics of Amyotrophic Lateral Sclerosis and Frontotemporal Dementia. Front. Neurosci. *14*, 42.

12. Ravits, J., Paul, P., and Jorg, C. (2007). Focality of upper and lower motor neuron degeneration at the clinical onset of ALS. Neurology *68*, 1571–1575.

13. Brettschneider, J., Del Tredici, K., Toledo, J.B., Robinson, J.L., Irwin, D.J., Grossman, M., Suh, E., Van Deerlin, V.M., Wood, E.M., Baek, Y., et al. (2013). Stages of pTDP-43 pathology in amyotrophic lateral sclerosis. Ann. Neurol. *74*, 20–38.

14. Hughes, J.T. (1982). Pathology of amyotrophic lateral sclerosis. Adv. Neurol. *36*, 61–74.

15. Nihei, K., McKee, A.C., and Kowall, N.W. (1993). Patterns of neuronal degeneration in the motor cortex of amyotrophic lateral sclerosis patients. Acta Neuropathol. *86*, 55–64.

16. Kim, E.-J., Sidhu, M., Gaus, S.E., Huang, E.J., Hof, P.R., Miller, B.L., DeArmond, S.J., and Seeley, W.W. (2016). Selective Frontoinsular von Economo Neuron and Fork Cell Loss in Early Behavioral Variant Frontotemporal Dementia. Cereb. Cortex *26*, 1843.

17. Santillo, A.F., Nilsson, C., and Englund, E. (2013). von Economo neurones are selectively targeted in frontotemporal dementia. Neuropathol. Appl. Neurobiol. *39*, 572–579.

18. Fajardo, C., Escobar, M.I., Buriticá, E., Arteaga, G., Umbarila, J., Casanova, M.F., and Pimienta, H. (2008). Von Economo neurons are present in the dorsolateral (dysgranular) prefrontal cortex of humans. Neurosci. Lett. *435*, 215–218.

19. González-Acosta, C.A., Escobar, M.I., Casanova, M.F., Pimienta, H.J., and Buriticá, E. (2018). Von Economo Neurons in the Human Medial Frontopolar Cortex. Front. Neuroanat. *12*, 64.

20. Cobos, I., and Seeley, W.W. (2015). Human von Economo Neurons Express Transcription Factors Associated with Layer V Subcerebral Projection Neurons. Cereb. Cortex *25*, 213–220.

21. Hodge, R.D., Miller, J.A., Novotny, M., Kalmbach, B.E., Ting, J.T., Bakken, T.E., Aevermann, B.D., Barkan, E.R., Berkowitz-Cerasano, M.L., Cobbs, C., et al. (2020). Transcriptomic evidence that von Economo neurons are regionally specialized extratelencephalic-projecting excitatory neurons. Nat. Commun. *11*, 1172.

22. Rivara, C.B., Sherwood, C.C., Bouras, C., and Hof, P.R. (2003). Stereologic characterization and spatial distribution patterns of Betz cells in the human primary motor cortex. Anat. Rec. A Discov. Mol. Cell. Evol. Biol. *270*, 137–151.

23. Allman, J.M., Tetreault, N.A., Hakeem, A.Y., Manaye, K.F., Semendeferi, K., Erwin, J.M., Park, S., Goubert, V., and Hof, P.R. (2011). The von Economo neurons in the frontoinsular and anterior cingulate cortex. Ann. N. Y. Acad. Sci. *1225*, 59–71.

24. Hodge, R.D., Bakken, T.E., Miller, J.A., Smith, K.A., Barkan, E.R., Graybuck, L.T., Close, J.L., Long, B., Johansen, N., Penn, O., et al. (2019). Conserved cell types with divergent features in human versus mouse cortex. Nature *573*, 61–68.

25. Molyneaux, B.J., Arlotta, P., Menezes, J.R.L., and Macklis, J.D. (2007). Neuronal subtype specification in the cerebral cortex. Nat. Rev. Neurosci. *8*, 427–437.

26. Zeng, H., Shen, E.H., Hohmann, J.G., Oh, S.W., Bernard, A., Royall, J.J., Glattfelder, K.J., Sunkin, S.M., Morris, J.A., Guillozet-Bongaarts, A.L., et al. (2012). Large-scale cellular-resolution gene profiling in human neocortex reveals species-specific molecular signatures. Cell *149*, 483–496.

27. Boldog, E., Bakken, T.E., Hodge, R.D., Novotny, M., Aevermann, B.D., Baka, J., Bordé, S., Close, J.L., Diez-Fuertes, F., Ding, S.-L., et al. (2018). Transcriptomic and morphophysiological evidence for a specialized human cortical GABAergic cell type. Nat. Neurosci. *21*, 1185–1195.

28. Humphrey, J., Venkatesh, S., Hasan, R., Herb, J.T., de Paiva Lopes, K., Küçükali, F., Byrska-Bishop, M., Evani, U.S., Narzisi, G., Fagegaltier, D., et al. (2023). Integrative transcriptomic analysis of the amyotrophic lateral sclerosis spinal cord implicates glial activation and suggests new risk genes. Nat. Neurosci. *26*, 150–162.

29. Prudencio, M., Belzil, V.V., Batra, R., Ross, C.A., Gendron, T.F., Pregent, L.J., Murray, M.E., Overstreet, K.K., Piazza-Johnston, A.E., Desaro, P., et al. (2015). Distinct brain transcriptome profiles in C9orf72-associated and sporadic ALS. Nat. Neurosci. *18*, 1175–1182.

30. Dickson, D.W., Baker, M.C., Jackson, J.L., DeJesus-Hernandez, M., Finch, N.A., Tian, S., Heckman, M.G., Pottier, C., Gendron, T.F., Murray, M.E., et al. (2019). Extensive transcriptomic study emphasizes importance of vesicular transport in C9orf72 expansion carriers. Acta Neuropathol. Commun. *7*, 150.

31. Subramanian, A., Tamayo, P., Mootha, V.K., Mukherjee, S., Ebert, B.L., Gillette, M.A., Paulovich, A., Pomeroy, S.L., Golub, T.R., Lander, E.S., and Mesirov, J.P. (2005). Gene set enrichment analysis: a knowledge-based approach for interpreting genome-wide expression profiles. Proc. Natl. Acad. Sci. USA *102*, 15545–15550.

32. Mohassel, P., Donkervoort, S., Lone, M.A., Nalls, M., Gable, K., Gupta, S.D., Foley, A.R., Hu, Y., Saute, J.A.M., Moreira, A.L., et al. (2021). Childhood amyotrophic lateral sclerosis caused by excess sphingolipid synthesis. Nat. Med. *27*, 1197–1204.

33. Verde, F., Otto, M., and Silani, V. (2021). Neurofilament Light Chain as Biomarker for Amyotrophic Lateral Sclerosis and Frontotemporal Dementia. Front. Neurosci. *15*, 679199.

34. Chou, C.C., Alexeeva, O.M., Yamada, S., Pribadi, A., Zhang, Y., Mo, B., Williams, K.R., Zarnescu, D.C., and Rossoll, W. (2015). PABPN1 suppresses TDP-43 toxicity in ALS disease models. Hum. Mol. Genet. *24*, 5154–5173.

35. Lee, S., Jun, Y.-W., Linares, G.R., Butler, B., Yuva-Adyemir, Y., Moore, J., Krishnan, G., Ruiz-Juarez, B., Santana, M., Pons, M., et al. (2023). Downregulation of Hsp90 and the antimicrobial peptide Mtk suppresses poly(GR)-induced neurotoxicity in C9ORF72-ALS/FTD. Neuron *111*, 1381–1390.e6.

36. Yamanaka, K., Chun, S.J., Boillee, S., Fujimori-Tonou, N., Yamashita, H., Gutmann, D.H., Takahashi, R., Misawa, H., and Cleveland, D.W. (2008). Astrocytes as determinants of disease progression in inherited amyotrophic lateral sclerosis. Nat. Neurosci. *11*, 251–253.

37. Dols-Icardo, O., Montal, V., Sirisi, S., López-Pernas, G., Cervera-Carles, L., Querol-Vilaseca, M., Muñoz, L., Belbin, O., Alcolea, D., Molina-Porcel, L., et al. (2020). Motor cortex transcriptome reveals microglial key events in amyotrophic lateral sclerosis. Neurol. Neuroimmunol. Neuroinflamm. *7*, e829.

38. Boillée, S., Yamanaka, K., Lobsiger, C.S., Copeland, N.G., Jenkins, N.A., Kassiotis, G., Kollias, G., and Cleveland, D.W. (2006). Onset and progression in inherited ALS determined by motor neurons and microglia. Science *312*, 1389–1392.

39. Kang, S.H., Li, Y., Fukaya, M., Lorenzini, I., Cleveland, D.W., Ostrow, L.W., Rothstein, J.D., and Bergles, D.E. (2013). Degeneration and impaired regeneration of gray matter oligodendrocytes in amyotrophic lateral sclerosis. Nat. Neurosci. *16*, 571–579.

40. Liddelow, S.A., Guttenplan, K.A., Clarke, L.E., Bennett, F.C., Bohlen, C.J., Schirmer, L., Bennett, M.L., Münch, A.E., Chung, W.S., Peterson,

T.C., et al. (2017). Neurotoxic reactive astrocytes are induced by activated microglia. Nature *541*, 481–487.

41. Habib, N., McCabe, C., Medina, S., Varshavsky, M., Kitsberg, D., Dvir-Szternfeld, R., Green, G., Dionne, D., Nguyen, L., Marshall, J.L., et al. (2020). Disease-associated astrocytes in Alzheimer's disease and aging. Nat. Neurosci. *23*, 701–706.
42. Zamanian, J.L., Xu, L., Foo, L.C., Nouri, N., Zhou, L., Giffard, R.G., and Barres, B.A. (2012). Genomic analysis of reactive astrogliosis. J. Neurosci. *32*, 6391–6410.
43. Keren-Shaul, H., Spinrad, A., Weiner, A., Matcovitch-Natan, O., Dvir-Szternfeld, R., Ulland, T.K., David, E., Baruch, K., Lara-Astaiso, D., Toth, B., et al. (2017). A Unique Microglia Type Associated with Restricting Development of Alzheimer's Disease. Cell *169*, 1276–1290.e17.
44. Fünfschilling, U., Supplie, L.M., Mahad, D., Boretius, S., Saab, A.S., Edgar, J., Brinkmann, B.G., Kassmann, C.M., Tzvetanova, I.D., Möbius, W., et al. (2012). Glycolytic oligodendrocytes maintain myelin and long-term axonal integrity. Nature *485*, 517–521.
45. Lappe-Siefke, C., Goebbels, S., Gravel, M., Nicksch, E., Lee, J., Braun, P.E., Griffiths, I.R., and Nave, K.-A. (2003). Disruption of Cnp1 uncouples oligodendroglial functions in axonal support and myelination. Nat. Genet. *33*, 366–374.
46. Griffiths, I., Klugmann, M., Anderson, T., Yool, D., Thomson, C., Schwab, M.H., Schneider, A., Zimmermann, F., McCulloch, M., Nadon, N., and Nave, K.A. (1998). Axonal swellings and degeneration in mice lacking the major proteolipid of myelin. Science *280*, 1610–1613.
47. Lee, Y., Morrison, B.M., Li, Y., Lengacher, S., Farah, M.H., Hoffman, P.N., Liu, Y., Tsingalia, A., Jin, L., Zhang, P.-W., et al. (2012). Oligodendroglia metabolically support axons and contribute to neurodegeneration. Nature *487*, 443–448.
48. Sweeney, M.D., Kisler, K., Montagne, A., Toga, A.W., and Zlokovic, B.V. (2018). The role of brain vasculature in neurodegenerative disorders. Nat. Neurosci. *21*, 1318–1331.
49. Miyazaki, K., Ohta, Y., Nagai, M., Morimoto, N., Kurata, T., Takehisa, Y., Ikeda, Y., Matsuura, T., and Abe, K. (2011). Disruption of neurovascular unit prior to motor neuron degeneration in amyotrophic lateral sclerosis. J. Neurosci. Res. *89*, 718–728.
50. Donnenfeld, H., Kascsak, R.J., and Bartfeld, H. (1984). Deposits of IgG and C3 in the spinal cord and motor cortex of ALS patients. J. Neuroimmunol. *6*, 51–57.
51. Garbuzova-Davis, S., Hernandez-Ontiveros, D.G., Rodrigues, M.C.O., Haller, E., Frisina-Deyo, A., Mirtyl, S., Sallot, S., Saporta, S., Borlongan, C.V., and Sanberg, P.R. (2012). Impaired blood-brain/spinal cord barrier in ALS patients. Brain Res. *1469*, 114–128.
52. Winkler, E.A., Sengillo, J.D., Sullivan, J.S., Henkel, J.S., Appel, S.H., and Zlokovic, B.V. (2013). Blood-spinal cord barrier breakdown and pericyte reductions in amyotrophic lateral sclerosis. Acta Neuropathol. *125*, 111–120.
53. Henkel, J.S., Beers, D.R., Wen, S., Bowser, R., and Appel, S.H. (2009). Decreased mRNA expression of tight junction proteins in lumbar spinal cords of patients with ALS. Neurology *72*, 1614–1616.
54. Zhou, K., Muroyama, A., Underwood, J., Leylek, R., Ray, S., Soderling, S.H., and Lechler, T. (2013). Actin-related protein2/3 complex regulates tight junctions and terminal differentiation to promote epidermal barrier formation. Proc. Natl. Acad. Sci. USA *110*, E3820–E3829.
55. Abu Taha, A., and Schnittler, H.-J. (2014). Dynamics between actin and the VE-cadherin/catenin complex: novel aspects of the ARP2/3 complex in regulation of endothelial junctions. Cell Adh. Migr. *8*, 125–135.
56. Braud, V.M., Allan, D.S., O'Callaghan, C.A., Söderström, K., D'Andrea, A., Ogg, G.S., Lazetic, S., Young, N.T., Bell, J.I., Phillips, J.H., et al. (1998). HLA-E binds to natural killer cell receptors CD94/NKG2A, B and C. Nature *391*, 795–799.
57. Coupel, S., Moreau, A., Hamidou, M., Horejsi, V., Soulillou, J.-P., and Charreau, B. (2007). Expression and release of soluble HLA-E is an immunoregulatory feature of endothelial cell activation. Blood *109*, 2806–2814.
58. Garofalo, S., Cocozza, G., Porzia, A., Inghilleri, M., Raspa, M., Scavizzi, F., Aronica, E., Bernardini, G., Peng, L., Ransohoff, R.M., et al. (2020). Natural killer cells modulate motor neuron-immune cell cross talk in models of Amyotrophic Lateral Sclerosis. Nat. Commun. *11*, 1773.
59. van Rheenen, W., van der Spek, R.A.A., Bakker, M.K., van Vugt, J.J.F.A., Hop, P.J., Zwamborn, R.A.J., de Klein, N., Westra, H.-J., Bakker, O.B., Deelen, P., et al. (2021). Common and rare variant association analyses in amyotrophic lateral sclerosis identify 15 risk loci with distinct genetic architectures and neuron-specific biology. Nat. Genet. *53*, 1636–1648.
60. Shin, J.E., Geisler, S., and DiAntonio, A. (2014). Dynamic regulation of SCG10 in regenerating axons after injury. Exp. Neurol. *252*, 1–11.
61. Khalil, M., Teunissen, C.E., Otto, M., Piehl, F., Sormani, M.P., Gattringer, T., Barro, C., Kappos, L., Comabella, M., Fazekas, F., et al. (2018). Neurofilaments as biomarkers in neurological disorders. Nat. Rev. Neurol. *14*, 577–589.
62. Jackson, J.L., Finch, N.A., Baker, M.C., Kachergus, J.M., DeJesus-Hernandez, M., Pereira, K., Christopher, E., Prudencio, M., Heckman, M.G., Thompson, E.A., et al. (2020). Elevated methylation levels, reduced expression levels, and frequent contractions in a clinical cohort of C9orf72 expansion carriers. Mol. Neurodegener. *15*, 7.
63. Miwa, J.M., Ibanez-Tallon, I., Crabtree, G.W., Sánchez, R., Sali, A., Role, L.W., and Heintz, N. (1999). lynx1, an endogenous toxin-like modulator of nicotinic acetylcholine receptors in the mammalian CNS. Neuron *23*, 105–114.
64. Miwa, J.M., Stevens, T.R., King, S.L., Caldarone, B.J., Ibanez-Tallon, I., Xiao, C., Fitzsimonds, R.M., Pavlides, C., Lester, H.A., Picciotto, M.R., and Heintz, N. (2006). The prototoxin lynx1 acts on nicotinic acetylcholine receptors to balance neuronal activity and survival in vivo. Neuron *51*, 587–600.
65. Oskarsson, B., Horton, D.K., and Mitsumoto, H. (2015). Potential Environmental Factors in Amyotrophic Lateral Sclerosis. Neurol. Clin. *33*, 877–888.
66. Lee, J.H., and Gleeson, J.G. (2010). The role of primary cilia in neuronal function. Neurobiol. Dis. *38*, 167–172.
67. Kanehisa, M., and Goto, S. (2000). KEGG: kyoto encyclopedia of genes and genomes. Nucleic Acids Res. *28*, 27–30.
68. Bulfone, A., Smiga, S.M., Shimamura, K., Peterson, A., Puelles, L., and Rubenstein, J.L. (1995). T-brain-1: a homolog of Brachyury whose expression defines molecularly distinct domains within the cerebral cortex. Neuron *15*, 63–78.
69. Han, W., Kwan, K.Y., Shim, S., Lam, M.M.S., Shin, Y., Xu, X., Zhu, Y., Li, M., and Sestan, N. (2011). TBR1 directly represses Fezf2 to control the laminar origin and development of the corticospinal tract. Proc. Natl. Acad. Sci. USA *108*, 3041–3046.
70. Kim, E.-J., Sidhu, M., Gaus, S.E., Huang, E.J., Hof, P.R., Miller, B.L., DeArmond, S.J., and Seeley, W.W. (2012). Selective frontoinsular von Economo neuron and fork cell loss in early behavioral variant frontotemporal dementia. Cereb. Cortex *22*, 251–259.
71. Nana, A.L., Sidhu, M., Gaus, S.E., Hwang, J.-H.L., Li, L., Park, Y., Kim, E.-J., Pasquini, L., Allen, I.E., Rankin, K.P., et al. (2019). Neurons selectively targeted in frontotemporal dementia reveal early stage TDP-43 pathobiology. Acta Neuropathol. *137*, 27–46.
72. Molyneaux, B.J., Arlotta, P., and Macklis, J.D. (2007). Molecular development of corticospinal motor neuron circuitry. 3–15; discussion. Novartis Found. Symp. *288*, 15–20. 96–98.
73. Bakken, T.E., Jorstad, N.L., Hu, Q., Lake, B.B., Tian, W., Kalmbach, B.E., Crow, M., Hodge, R.D., Krienen, F.M., Sorensen, S.A., et al. (2021).

Comparative cellular analysis of motor cortex in human, marmoset and mouse. Nature *598*, 111–119.

74. Yang, L., Yang, Y., Yuan, J., Sun, Y., Dai, J., and Su, B. (2019). Transcriptomic Landscape of von Economo Neurons in Human Anterior Cingulate Cortex Revealed by Microdissected-Cell RNA Sequencing. Cereb. Cortex *29*, 838–851.
75. Gigante, E.D., Taylor, M.R., Ivanova, A.A., Kahn, R.A., and Caspary, T. (2020). ARL13B regulates Sonic hedgehog signaling from outside primary cilia. eLife *9*, e50434.
76. Revenkova, E., Liu, Q., Gusella, G.L., and Iomini, C. (2018). The Joubert syndrome protein ARL13B binds tubulin to maintain uniform distribution of proteins along the ciliary membrane. J. Cell Sci. *131*, jcs212324.
77. Yadav, A., Matson, K.J.E., Li, L., Hua, I., Petrescu, J., Kang, K., Alkaslasi, M.R., Lee, D.I., Hasan, S., Galuta, A., et al. (2023). A cellular taxonomy of the adult human spinal cord. Neuron *111*, 328–344.e7.
78. Gami-Patel, P., van Dijken, I., van Swieten, J.C., Pijnenburg, Y.A.L., Netherlands Brain Bank, Rozemuller, A.J.M., Hoozemans, J.J.M., and Dijkstra, A.A. (2019). Von Economo neurons are part of a larger neuronal population that are selectively vulnerable in C9orf72 frontotemporal dementia. Neuropathol. Appl. Neurobiol. *45*, 671–680.
79. Gami-Patel, P., Scarioni, M., Bouwman, F.H., Boon, B.D.C., van Swieten, J.C., Brain Bank, N., Rozemuller, A.J.M., Smit, A.B., Pijnenburg, Y.A.L., Hoozemans, J.J.M., and Dijkstra, A.A. (2022). The severity of behavioural symptoms in FTD is linked to the loss of GABRQ-expressing VENs and pyramidal neurons. Neuropathol. Appl. Neurobiol. *48*, e12798.
80. Gelon, P.A., Dutchak, P.A., and Sephton, C.F. (2022). Synaptic dysfunction in ALS and FTD: anatomical and molecular changes provide insights into mechanisms of disease. Front. Mol. Neurosci. *15*, 1000183.
81. Gao, F.-B., Almeida, S., and Lopez-Gonzalez, R. (2017). Dysregulated molecular pathways in amyotrophic lateral sclerosis-frontotemporal dementia spectrum disorder. EMBO J. *36*, 2931–2950.
82. Zhang, Y.-J., Guo, L., Gonzales, P.K., Gendron, T.F., Wu, Y., Jansen-West, K., O'Raw, A.D., Pickles, S.R., Prudencio, M., Carlomagno, Y., et al. (2019). Heterochromatin anomalies and double-stranded RNA accumulation underlie poly(PR) toxicity. Science *363*, eaav2606.
83. Yu, C.-H., Davidson, S., Harapas, C.R., Hilton, J.B., Mlodzianoski, M.J., Laohamonthonkul, P., Louis, C., Low, R.R.J., Moecking, J., De Nardo, D., et al. (2020). TDP-43 Triggers Mitochondrial DNA Release via mPTP to Activate cGAS/STING in ALS. Cell *183*, 636–649.e18.
84. Kim, J.C., Badano, J.L., Sibold, S., Esmail, M.A., Hill, J., Hoskins, B.E., Leitch, C.C., Venner, K., Ansley, S.J., Ross, A.J., et al. (2004). The Bardet-Biedl protein BBS4 targets cargo to the pericentriolar region and is required for microtubule anchoring and cell cycle progression. Nat. Genet. *36*, 462–470.
85. Wheway, G., Schmidts, M., Mans, D.A., Szymanska, K., Nguyen, T.-M.T., Racher, H., Phelps, I.G., Toedt, G., Kennedy, J., Wunderlich, K.A., et al. (2015). An siRNA-based functional genomics screen for the identification of regulators of ciliogenesis and ciliopathy genes. Nat. Cell Biol. *17*, 1074–1087.
86. van Rheenen, W., Shatunov, A., Dekker, A.M., McLaughlin, R.L., Diekstra, F.P., Pulit, S.L., van der Spek, R.A.A., Võsa, U., de Jong, S., Robinson, M.R., et al. (2016). Genome-wide association analyses identify new risk variants and the genetic architecture of amyotrophic lateral sclerosis. Nat. Genet. *48*, 1043–1048.
87. Keenan, A.B., Torre, D., Lachmann, A., Leong, A.K., Wojciechowicz, M.L., Utti, V., Jagodnik, K.M., Kropiwnicki, E., Wang, Z., and Ma'ayan, A. (2019). ChEA3: transcription factor enrichment analysis by orthogonal omics integration. Nucleic Acids Res. *47*, W212–W224.
88. Mall, M., Kareta, M.S., Chanda, S., Ahlenius, H., Perotti, N., Zhou, B., Grieder, S.D., Ge, X., Drake, S., Euong Ang, C., et al. (2017). Myt1l safeguards neuronal identity by actively repressing many non-neuronal fates. Nature *544*, 245–249.
89. Conaco, C., Otto, S., Han, J.-J., and Mandel, G. (2006). Reciprocal actions of REST and a microRNA promote neuronal identity. Proc. Natl. Acad. Sci. USA *103*, 2422–2427.
90. Horton, J.D., Goldstein, J.L., and Brown, M.S. (2002). SREBPs: activators of the complete program of cholesterol and fatty acid synthesis in the liver. J. Clin. Invest. *109*, 1125–1131.
91. Egawa, N., Izumi, Y., Suzuki, H., Tsuge, I., Fujita, K., Shimano, H., Izumikawa, K., Takahashi, N., Tsukita, K., Enami, T., et al. (2022). TDP-43 regulates cholesterol biosynthesis by inhibiting sterol regulatory element-binding protein 2. Sci. Rep. *12*, 7988.
92. Liu, S., Trupiano, M.X., Simon, J., Guo, J., and Anton, E.S. (2021). The essential role of primary cilia in cerebral cortical development and disorders. Curr. Top. Dev. Biol. *142*, 99–146.
93. Juric-Sekhar, G., Adkins, J., Doherty, D., and Hevner, R.F. (2012). Joubert syndrome: brain and spinal cord malformations in genotyped cases and implications for neurodevelopmental functions of primary cilia. Acta Neuropathol. *123*, 695–709.
94. Thrupp, N., Sala Frigerio, C., Wolfs, L., Skene, N.G., Fattorelli, N., Poovathingal, S., Fourne, Y., Matthews, P.M., Theys, T., Mancuso, R., et al. (2020). Single-Nucleus RNA-Seq Is Not Suitable for Detection of Microglial Activation Genes in Humans. Cell Rep. *32*, 108189.
95. Mohammadi, S., Davila-Velderrain, J., and Kellis, M. (2020). A multiresolution framework to characterize single-cell state landscapes. Nat. Commun. *11*, 5399.
96. Haghverdi, L., Lun, A.T.L., Morgan, M.D., and Marioni, J.C. (2018). Batch effects in single-cell RNA-sequencing data are corrected by matching mutual nearest neighbors. Nat. Biotechnol. *36*, 421–427.
97. Ritchie, M.E., Phipson, B., Wu, D., Hu, Y., Law, C.W., Shi, W., and Smyth, G.K. (2015). limma powers differential expression analyses for RNA-sequencing and microarray studies. Nucleic Acids Res. *43*, e47.
98. Leek, J.T., and Storey, J.D. (2007). Capturing heterogeneity in gene expression studies by surrogate variable analysis. PLoS Genet. *3*, 1724–1735.
99. Korotkevich, G., Sukhov, V., Budin, N., Shpak, B., Artyomov, M.N., and Sergushichev, A. (2021). Fast gene set enrichment analysis. Preprint at bioRxiv, 060012.
100. de Leeuw, C.A., Mooij, J.M., Heskes, T., and Posthuma, D. (2015). MAGMA: generalized gene-set analysis of GWAS data. PLoS Comput. Biol. *11*, e1004219.
101. Murphy, A.E., Schilder, B.M., and Skene, N.G. (2021). MungeSumstats: a Bioconductor package for the standardization and quality control of many GWAS summary statistics. Bioinformatics *37*, 4593–4596.
102. Zhang, M.J., Hou, K., Dey, K.K., Sakaue, S., Jagadeesh, K.A., Weinand, K., Taychameekiatchai, A., Rao, P., Pisco, A.O., Zou, J., et al. (2022). Polygenic enrichment distinguishes disease associations of individual cells in single-cell RNA-seq data. Nat. Genet. *54*, 1572–1580.
103. Schindelin, J., Arganda-Carreras, I., Frise, E., Kaynig, V., Longair, M., Pietzsch, T., Preibisch, S., Rueden, C., Saalfeld, S., Schmid, B., et al. (2012). Fiji: an open-source platform for biological-image analysis. Nat. Methods *9*, 676–682.
104. Cairns, N.J., Bigio, E.H., Mackenzie, I.R.A., Neumann, M., Lee, V.M.-Y., Hatanpaa, K.J., White, C.L., Schneider, J.A., Grinberg, L.T., Halliday, G., et al. (2007). Neuropathologic diagnostic and nosologic criteria for frontotemporal lobar degeneration: consensus of the Consortium for Frontotemporal Lobar Degeneration. Acta Neuropathol. *114*, 5–22.
105. Mackenzie, I.R.A., Neumann, M., Baborie, A., Sampathu, D.M., Du Plessis, D., Jaros, E., Perry, R.H., Trojanowski, J.Q., Mann, D.M.A., and Lee, V.M.Y. (2011). A harmonized classification system for FTLD-TDP pathology. Acta Neuropathol. *122*, 111–113.

106. Mann, D.M.A., Rollinson, S., Robinson, A., Bennion Callister, J., Thompson, J.C., Snowden, J.S., Gendron, T., Petrucelli, L., Masuda-Suzukake, M., Hasegawa, M., et al. (2013). Dipeptide repeat proteins are present in the p62 positive inclusions in patients with frontotemporal lobar degeneration and motor neurone disease associated with expansions in C9ORF72. Acta Neuropathol. Commun. *1*, 68.

107. Lee, H., Fenster, R.J., Pineda, S.S., Gibbs, W.S., Mohammadi, S., Davila-Velderrain, J., Garcia, F.J., Therrien, M., Novis, H.S., Gao, F., et al. (2020). Cell Type-Specific Transcriptomics Reveals that Mutant Huntingtin Leads to Mitochondrial RNA Release and Neuronal Innate Immune Activation. Neuron *107*, 891–908.e8.

108. Mohammadi, S., Ravindra, V., Gleich, D.F., and Grama, A. (2018). A geometric approach to characterize the functional identity of single cells. Nat. Commun. *9*, 1516.

109. Traag, V.A., Waltman, L., and van Eck, N.J. (2019). From Louvain to Leiden: guaranteeing well-connected communities. Sci. Rep. *9*, 5233.

110. Cutler, A., and Breiman, L. (1994). Archetypal Analysis. Technometrics *36*, 338–347.

111. Brin, S., and Page, L. (1998). The anatomy of a large-scale hypertextual Web search engine. Comput. Netw. ISDN Syst. *30*, 107–117.

STAR★METHODS

KEY RESOURCES TABLE

REAGENT or RESOURCE	SOURCE	IDENTIFIER
Antibodies		
Rabbit polyclonal anti-ArpC3	LSBio	Cat# LS-C409316;
Mouse monoclonal anti-Claudin-5	Thermo Fisher Scientific	Cat# 352500; RRID: AB_2533200
Mouse monoclonal anti-HLA-E	Proteintech	Cat# 66530-1-Ig; RRID: AB_2881893
Guinea pig polyclonal anti-NeuN	Synaptic Systems	Cat# 266004; RRID: AB_2619988
Mouse monoclonal Anti-OCT6 (POU3F1)	MilliporeSigma	Cat# MABN738; RRID: AB_2876862
Mouse monoclonal anti-pTDP-43 pS409/410	Cosmo Bio	Cat# CAC-TIP-PTD-M01; RRID: AB_1961900
Rabbit polyclonal anti-VAT1L	Thermo Fisher Scientific	Cat# PA5-98934; RRID: AB_2813547
Goat polyclonal anti-VE-cadherin	R&D Systems	Cat# AF938; RRID: AB_355726
Biological samples		
Human post-mortem brain samples	Mayo Clinic Neuropathology Laboratory	N/A
Chemicals, peptides, and recombinant proteins		
OptiPrep Density Gradient Medium (Iodixanol)	MilliporeSigma	Cat# D1556
SUPERase-In RNase Inhibitor	Thermo Fisher Scientific	Cat# AM2696
Lycopersicon Esculentum (Tomato) lectin DyLight 488	Vector Laboratories	Cat# DL-1174-1
TrueBlack Lipofuscin Autofluorescence Quencher	Biotium	Cat# 23007
3,3'-Diaminobenzidine	MilliporeSigma	Cat# D12384
Critical commercial assays		
Chromium Next GEM Single Cell 3' Kit v3.1	10x Genomics	Cat# 1000268
Chromium Next GEM Chip G Single Cell Kit	10x Genomics	Cat# 1000120
Dual Index Kit TT Set A	10x Genomics	Cat# 1000215
Vector Blue Substrate Kit, Alkaline Phosphatase	Vector Laboratories	Cat# SK-5300
Deposited data		
Raw sequencing data	This study	NCBI SRA: PRJNA1073234
Processed gene expression counts	This study	Synapse: syn51105515
Metadata, tables of results, and supplemental data	This study	Synapse: syn51105515
ALS GWAS European summary statistics	van Rheenen et al.[59]	https://www.ebi.ac.uk/gwas/studies/GCST90027164
Experimental models: Organisms/strains		
Mouse: C57BL/6J	The Jackson Laboratory	Cat #: 000664; RRID: IMSR_JAX:000664
Software and algorithms		
Cell Ranger	10x Genomics	https://www.10xgenomics.com/support/software/cell-ranger/latest
ACTIONet	Mohammadi et al.[95]	https://github.com/decomverse/ACTIONet
Batchelor	Haghverdi et al.[96]	https://bioconductor.org/packages/release/bioc/html/batchelor.html
limma	Ritchie et al.[97]	https://bioconductor.org/packages/release/bioc/html/limma.html
SVA	Leek and Storey[98]	https://bioconductor.org/packages/release/bioc/html/sva.html
fgsea	Korotkevich et al.[99]	https://bioconductor.org/packages/release/bioc/html/fgsea.html
ChEA3	Keenan et al.[87]	https://maayanlab.cloud/chea3/

(*Continued on next page*)

Continued

REAGENT or RESOURCE	SOURCE	IDENTIFIER
MAGMA	de Leeuw et al.[100]	https://ctg.cncr.nl/software/magma
MungeSumstats	Murphy et al.[101]	https://github.com/neurogenomics/MungeSumstats
scDRS	Zhang et al.[102]	https://github.com/martinjzhang/scDRS
FIJI	Schindelin et al.[103]	https://imagej.net/software/fiji/
Other		
KIMBLE KONTES Dounce tissue grinder, 2 mL	DKW Life Sciences	Cat# 885300-0002
Chromium Controller	10x Genomics	Cat# 1000202

RESOURCE AVAILABILITY

Lead contact

Further information and requests for resources and reagents should be directed to the lead contact, Myriam Heiman (mheiman@mit.edu).

Materials availability

This study did not generate new unique reagents.

Data and code availability

- All raw sequencing data has been deposited to the NIH NCBI Sequence Read Archive (SRA) under BioProject accession PRJNA1073234.
- All processed count matrices, full tables of results, and other supplemental data have been made available on Synapse (Project SynID: syn51105515). These data can be accessed at https://www.synapse.org/#!Synapse:syn51105515.
- Code used to for snRNA-seq data processing, quality control, and cell type identification is available from https://github.com/decomverse/ACTIONet.
- Additional information regarding donor samples and data analysis, as well as code required to reanalyze the data reported in this paper, may be obtained from the lead contact upon reasonable request.
- Additional clinical, pathological, and genotype information pertaining to human samples can be provided upon reasonable request from the lead contact.

EXPERIMENTAL MODEL AND SUBJECT DETAILS

Data reporting

Statistical methods were not used to predetermine the sample size.

Human samples

Human tissue analysis was conducted as exempt human research. Fresh-frozen post-mortem brain samples were obtained from the Mayo Clinic Neuropathology Laboratory (Jacksonville, FL USA). All cases were carefully analyzed by an experienced and certified neuropathologist, and a final neuropathology diagnosis was available for all samples. TDP-43 pathology was confirmed in all ALS and FTLD samples used for our studies based upon current consensus criteria, which investigates cortical and subcortical distribution of TDP-43 neuropathologic inclusions.[104,105] A section of the cerebellum was screened for *C9orf72*-related pathology with P62 immunohistochemistry,[106] and repeat expansions in all *C9orf72*-associated cases were confirmed via Southern blot. All samples were carefully genotyped before being selected for our studies. Sporadic cases contained no positive family history of either ALS or FTLD and had no defined genetic risk factors (no mutation in *SOD1*, *TARDBP*, *FUS*, *C9orf72*, *NEK1*, *GRN*, *MAPT*, or *TBK1*). *C9orf72*+ cases were also negative for mutations in the other genes listed. Extent of upper and lower motor neuron involvement was investigated in all samples using Luxol fast blue and IBA-1 immunohistochemistry in the motor cortex, midbrain, and medulla. Diagnosis of motor neuron disease was positive for all ALS and negative for all FTLD and control samples selected. Criteria for exclusion from consideration included noticeable discoloration from prolonged hypoxia, or a pathology report that suggested potentially confounding non-ALS/FTLD neurological pathology, or neurological cause of death in control cases. We included a total of 73 individuals: 17 sporadic ALS (8 male; 9 female), 16 *C9orf72* familial ALS (6 male; 10 female), 13 sporadic FTLD (7 male; 6 female), 11 *C9orf72* familial FTLD (6 male; 5 female) and 16 pathologically normal (8 male; 8 female).

Animals

All mouse experimental procedures were conducted with the approval of the Massachusetts Institute of Technology Animal Care and Use Committee. Mouse studies were conducted on 8-week-old male C57BL/6J mice (The Jackson Laboratory, Strain# 000664). Mice were housed under pathogen-free conditions, with food and water provided *ad libitum* on a standard 12h light/12h dark cycle. No procedures were performed on the mice prior to the outlined experiments.

METHOD DETAILS

Human sample preparation

All cases underwent standard neuroanatomic sampling by a single neuropathologist (D.W.D) who performed the cutting of all autopsied procured brains (Mayo Clinic IRB 15-009452). For all brains harvested and received at the Mayo Clinic Neuropathology Laboratory, the right hemibrain was frozen (-80°C) and the left hemibrain was fixed for long-term preservation. For the single-nucleus study, BA9 (dorsolateral prefrontal) and BA4 (primary motor) were sampled from frozen tissue stored at -80°C. To maintain tissue integrity, tissue was stored at -20°C for 30 min and subsequently at room temperature for 45 min to allow gradual thawing prior to sampling. BA9 was sampled from the lateral surface in cases with an intact hemisphere, or at the level of the head of the caudate in coronal slabs. BA4 was sampled from the lateral surface in cases with an intact hemisphere, or at the level of the pulvinar in coronal slabs. For IHC, sections of BA4 and BA9 from the fixed hemibrain were used.

Mouse sample preparation

Mice were euthanized by decapitation and the whole brain was dissected on dry ice. Brain tissue was placed onto a chilled stainless-steel matrix and cut coronally at the apex of the dorsal side. A 1.5mm punch biopsy with plunger was used to collect motor cortex tissue. Tissue dissections were immediately submerged in a homogenization buffer for nuclear isolation.

Isolation of nuclei from post-mortem fresh frozen human and fresh mouse brain tissue

Nuclei isolation was performed as reported in Lee et al.[107] All procedures were performed on ice. For the human tissue samples, 150 mg of grey matter was sectioned and homogenized. Briefly, each tissue was homogenized in 700 μL of homogenization buffer with a 2 mL tissue grinder using 10 strokes with a loose pestle, followed by 10 strokes with a tight pestle. Homogenized tissue was filtered through a 40 μm cell strainer and mixed with 450 μL of working solution. The mixture was then slowly pipetted onto the top of an iodixanol density gradient (300 μL 40% solution and 750 μL of 30% solution) inside a dolphin microcentrifuge tube. Nuclei were pelleted at the 30%-40% interface of the density gradient by centrifugation at 10,000 x *g* for 5 min at 4°C using a fixed angle rotor. The nuclear pellet was collected by aspirating ~100μL from the interface and transferring to a 1.5 mL siliconized microcentrifuge tube. The pellet was washed with in PBS with 2% BSA containing 0.12 U/μL SUPERase-In RNase Inhibitor (Thermo Fisher Scientific). The nuclei were pelleted by centrifugation at 300 x *g* for 3 min at 4°C using a swing-bucket rotor. The nuclei were again pelleted and washed twice more under the same conditions. The nuclear pellet was resuspended in 100 μL of PBS with 2% BSA.

Library preparation and sequencing

Droplet-based snRNA sequencing libraries were prepared using the Chromium Next GEM Single Cell 3′ reagent kit v3.1 (10x Genomics) according to the manufacturer's protocol, targeting 7,000 nuclei per sample. Libraries were sequenced on a NovaSeq 6000 at the Broad Institute Genomics Platform.

Sequencing data preprocessing

Cell Ranger v6.0 (10x Genomics) was used for genome alignment and feature-barcode matrix generation. Reads were aligned to the human reference genome GRCh38 or mouse reference genome mm10 allowing mapping to intronic regions.

Immunofluorescent labeling and confocal microscopy

Fresh-frozen tissues from the right hemibrain were embedded in NEG-50 (Epredia) and cryo-sectioned onto glass slides at 20 μm thickness. Sections were dried at room temperature in a humidity chamber for 5 min and then fixed with cold acetone for 10 min under gentle agitation. Slides were washed with 1X TBS, permeabilized with 1X TBS-T (1X TBS supplemented with 0.05% Tween-20) for 15 min and blocked with blocking buffer (2% heat-inactivated donkey serum, 0.1% fish gelatin in 1X TBS-T) for 1 hour at room temperature. Combinations of primary antibodies and/or fluorescently labeled lectin were incubated on slides in blocking buffer overnight at 4 °C with the following dilutions: claudin-5 (Thermo Fisher Scientific, Cat# 352500; 1:200), ArpC3 (LSBio, Cat# LS-C409316; 1:100), VE-cadherin (R&D Systems, Cat# AF938; 1:200), HLA-E (Proteintech, Cat# 66530-1-Ig; 1:200), POU3F1 (MilliporeSigma, Cat# MABN738; 1:200), NeuN (Synaptic Systems, Cat# 266004; 1:1000), and DyLight 488 labeled tomato lectin (Vector Laboratories, Cat# DL-1174-1; 1:50). The next day, slides were washed with 1X TBS, and incubated in Alexa Fluor-conjugated secondary antibodies (Thermo Fisher Scientific) diluted 1:500 in blocking buffer for 1 hour at room temperature. After washing with 1X TBS, slides were treated with TrueBlack Lipofuscin Autofluorescence Quencher (Biotium) for 30 seconds to reduce

autofluorescence. Slides were counterstained with DAPI and mounted with ProLong Gold antifade mounting media (Thermo Fisher Scientific). A STELLARIS 5 confocal microscope (Leica Microsystems) with a 63X objective lens was used for imaging across the entire section thickness using a step size of 0.3 μm.

Immunofluorescent image quantification

Image processing was performed on sum projections in FIJI[103] and blinded to experimental group.

ArpC3/lectin co-labeling

ArpC3, lectin, and DAPI were co-stained to compare ArpC3 protein expression between the PN and SALS endothelium in the motor cortex. Lectin selectively labels blood vessels and was used to manually trace microvessels and thus quantify only vascular ArpC3 fluorescence. The average per pixel fluorescence intensity of three randomly selected avascular 40 x 40-micron regions was subtracted from the per pixel intensity of ArpC3 fluorescence in each lectin-positive microvessel to correct for differences in tissue autofluorescence across samples. Vascular ArpC3 fluorescence was then averaged across at least 16 microvessels per sample and normalized to 1 for PN cases. Quantification of vascular lectin and ArpC3 immunofluorescence signal is relative to PN. Comparisons were conducted across $n = 5$ PN and $n = 5$ SALS donor individuals. Statistical significance was determined using an unpaired one-tailed *t*-test. An identical approach was used to compare HLA-E protein expression across $n = 6$ PN and $n = 6$ SALS donor individuals.

Claudin-5/VE-cadherin co-labeling

Claudin-5, VE-cadherin, and DAPI were co-stained to assess junctional localization in the PN and SALS endothelium in the motor cortex. Quantification represents the percentage of blood vessels with junctional localization of claudin-5 and VE-cadherin. Junctional localization is defined as visible strands of claudin-5 or VE-cadherin immunofluorescence in VE-cadherin positive microvessels. Comparisons were conducted across $n = 5$ PN and $n = 5$ SALS donor individuals. Statistical significance was determined using an unpaired one-tailed *t*-test.

Immunohistochemistry and stereology

Formalin-fixed, paraffin-embedded tissues from the left hemibrain of MCX, DLPFC, and ACC were sectioned at 5 μm thickness and mounted on glass slides. Sections were dried at 60°C overnight. All tissues were from cases used in the snRNA-seq study.

VAT1L/TDP-43 co-labeling

Immunostaining was performed on the Thermo Scientific Autostainer 480S, using the Envision G/2 double stain kit (Dako). Horseradish peroxidase (HRP) labeling of mouse monoclonal anti-phospho-TDP-43 antibody (pTDP-43 pS409/410) (Cosmo Bio, Cat# CAC-TIP-PTD-M01; 1:5000) was visualized using 3,3'-diaminobenzidine (DAB+) as the chromogen. Alkaline phosphatase labeling of rabbit polyclonal anti-VAT1L antibody (Thermo Fisher Scientific, Cat# PA5-98934; 1:500) was visualized using DAB+ and Vector Blue Alkaline Phosphatase Substrate kit (Vector Laboratories).

VAT1L stereology

From 59 donor individuals (SALS $n = 14$, C9ALS $n = 12$, SFTLD $n = 11$, C9FTLD $n = 7$, PN $n = 15$), sections of MCX and PFC from each case were immunostained with rabbit polyclonal anti-VAT1L antibody (Thermo Fisher Scientific, Cat# PA5-98934; 1:500) and visualized using DAB+. Layer 5 cells were manually counted (two counts per slide) by a trained and blinded individual, with accepted intra-count variability of less than 5%. VAT1L+ cells were not observed outside of layer 5. Betz cells were identified by laminar distribution, soma size, nucleus size, prominent nucleolus, and distinct cytosolic VAT1L staining pattern. Panoramic pictures of the slides were obtained to measure the gray matter area using FIJI. The number of cells per area (cells/mm^2) was obtained by dividing the mean of the number of cells per count by the measured gray matter area. Statistical significance for each comparison was determined using an unpaired one-tailed *t*-test.

QUANTIFICATION AND STATISTICAL ANALYSIS

Cell clustering and curation

We used the ACTIONet[95,108] R package for data cleaning, batch correction, clustering, imputation, and cell type annotation as in Lee et al. with some modifications.[107] In brief, raw count matrices were prefiltered by removing barcodes containing less than 700 unique genes or greater than 20% mtRNA content. Counts were depth-normalized across samples and log-transformed using the batchelor R package.[96] Further per-cluster filtering was performed by iteratively removing cells with abnormally low or high RNA content (relative to the distribution of the specific cluster), ambiguous overlapping profiles resembling dissimilar cell types (generally corresponding to doublet nuclei), and cells corresponding to graph nodes with a low *k*-core or low centrality in the cell-cell similarity network (generally corresponding to high ambient RNA content or doublet nuclei). We also filtered cells overexpressing immediate early genes (e.g. *FOS*, *JUN*, *JUNB*, *JUND*) not correlated with phenotype, and indicative of hypoxia or cell damage. Following this rigorous filtering regime, we retained 625,973 unique cellular profiles corresponding to ~8,500 post-quality control nuclei per donor, with an average of ~14,000 unique transcripts, ~4,200 unique genes, and mtRNA content of 1.48% per nucleus (Figure S1B)

Cell type annotation

A curated set of known major cell type markers was used to annotate individual cells with their expected cell type and assign a confidence score to each annotation. For ill-characterized or ambiguous subpopulations, we assigned identity based on visually distinct,

well-defined gene expression domains reproducibly identified by Leiden[109] and archetypal analysis[110] clustering at multiple resolutions. Descriptive labels were determined by the unique co-expression of marker genes identified by ACTIONet for each cluster.

Alternative annotations

The choice of cell type annotations is an important element of experimental design that can impact the results and interpretation of a profiling study such as this. The annotations presented here are not intended to serve as a rigorous characterization of the transcriptional landscape of the motor or prefrontal cortices, as this has already been done.[24,73] Rather, the number and choice of annotated clusters in this study reflects the focus on known or novel cell populations that are or may be implicated in ALS and FTLD pathobiology. This is further constrained by the need to obtain not only a suitable number of cells per cluster and per donor, but also have representation from as many individual donors as possible within each cluster to conduct rigorous statistical analyses. For this reason, we chose a course clustering resolution that non-redundantly captures disease-associated responses and relevant populations that are important in the context of our study, and that previous studies do not resolve, yet are central to some of our findings. We understand that other researchers may wish to use the data generated in this study with different goals in mind. Therefore, we have included the equivalent cell-level annotations published in Bakken et al. (Nature 2021)[73] as a set of secondary cell-level annotations (Figure S1K) to facilitate integration and comparison with other similar datasets.

To perform the label transfer we used the ACTIONet R package to generate a marker set from the Bakken human M1 dataset which was then used to annotate the cells in our dataset. The accuracy of the label transfer was manually verified. These annotations can be found in the metadata column titled ‘‘Bakken_M1’’ in the processed and annotated data available on Synapse.

Differential gene expression analysis

We employed a pseudo-bulk approach considering each donor individual as a single biological replicate. For the pan-neuronal analysis, neuronal subtypes were aggregated into excitatory and inhibitory classes. For the cell type-specific analysis, rare subclusters that lacked sufficient representation were merged if they were similar enough to still reasonably be classified as one cell type. More specifically, rare clusters were merged if their subclusters were directly adjacent and belonged to the same supercluster (e.g. subclusters of PV neurons or the two L5 *VAT1L*+ subtypes) and could not be analyzed independently. Specifics on how clusters were aggregated for both analyses are detailed in Table S3 and are visualized in Figure S1L. We required that a cluster be represented across at least 4 disease and 4 control individuals, separately for each disease and brain region, and with at least 20 cells per individual. If this criterion could not be met and rare clusters could not be merged with a larger group, these clusters were excluded from analysis. The following clusters were excluded from most analyses based on these criteria: In SOM *SST NPY*, In 5HT3aR *CDH4 SCGN*, In 5HT3aR *CDH4 CCK*, Vasc Fibro *CLMP KCNMA1*. These clusters comprised 2815 cells, or 0.45% of the data.

For each differential expression cluster, only genes present in at least 10% of cells were retained for analysis. Counts were depth normalized, scaled by library-size, and $\log_2$-transformed. Pseudo-bulk expression profiles were computed by averaging normalized log-counts within each cluster for each unique sample. We used surrogate variable analysis[98] (implemented in the SVA R package) to identify and remove sources of unknown variance. Pseudo-bulk differential gene expression analysis was performed using the limma R package.[97] We found Braak stage and Thal phase to be poor predictors of gene expression and omitted them from the design formula.

In all figures showing DEG results, the magnitude of gene expression change is reported as the Z score of the $\log_2$-fold change (LFCs) centered at 0. LFCs were converted to Z scores per cell type using the R function scale(x,center=0,scale=sd(x)), where x is the vector of LFCs. Genes were considered differentially expressed if they had a Z score > 1, and a false discovery rate (FDR)-corrected p value < 0.05. To ensure that these results were robust and confirm that our chosen thresholds were reasonable, we performed permutation testing whereby we randomly shuffled covariate labels and repeated the pseudo-bulk analysis. This analysis estimated the number of genes that would be classified as differentially expressed by chance (i.e. false positives). In all cases, zero or close to zero DEGs were detected.

Pathway enrichment analysis

Pathway enrichment analysis was performed with Gene Set Enrichment Analysis[31] using the FGSEA R package,[99] and queried against the relevant databases. For pathway enrichment analysis of DEGs, we used $-\log_{10}$(p value)*sign(LFC) as the ranking metric, and for pathway enrichment of TxD-associated genes, we used $-\log_{10}$(p value)*sign(ρ), where ρ is the correlation coefficient. In all panels, we report the normalized enrichment score (NES) and nominal $\log_{10}$(p value) of enrichment.

Predicting upstream regulators

Upstream transcription factors of statistically significant DEGs and TxD-associated genes were determined using ChEA3,[87] which runs enrichment tests against multiple transcription factor libraries. We exclusively report the mean rank results, which represent the aggregate average ranking across all ChEA3 libraries.

Cross-region and cross-species comparisons

For each PN donor individual and mouse, pseudo-bulked gene expression profiles for each transcriptional subtype were generated by averaging log-normalized counts. The mean expression of the pseudo-bulked profiles was used to compute the pairwise

Pearson's correlation of transcriptome-wide gene expression across subtypes of MCX and PFC in human (Figure 1F) and between MCX of human and mouse (Figure S5B). For cross-species comparisons, only expression values of homologous genes were used to compute the correlation. To minimize the contribution of ubiquitous housekeeping genes and to amplify the contribution of cell type-specific signal, we regressed out the mean gene expression profile across all subtypes from the expression matrices before computing the correlation.

Preprocessing pseudo-bulk expression for multiple analyses

For correlation analyses (Figure 2A), TxD score calculation (Figure 4C), and TxD association analyses (Figures 4E and S3A-S3D) we generated normalized, covariate-corrected pseudo-bulk expression profiles for each transcriptional subtype. We incorporated the same covariates as in the DEG analysis and used SVA to remove unwanted variance. These corrected expression profiles were used as input for each analysis.

Calculation of transcriptional divergence scores

The TxD score is a quantification of transcriptional dysregulation. It represents the change in transcriptome-wide gene expression of each subtype in disease from its respective PN expression profile. The divergence score is the Euclidean distance between the median disease and corresponding PN covariate-corrected, pseudo-bulk expression profiles for each cell type.

Scoring TxD association

To identify genes whose (co-)expression is correlated with transcriptional dysregulation, we used the covariate-corrected, pseudo-bulk expression profile for each cluster in PN cases, which represents the mean endogenous expression of all genes per transcriptional subtype among control samples. For each gene, we computed the Spearman correlation and correlation p value of gene expression vs. TxD score per cluster for each disease and brain region, giving us a score and ranking of every gene in the transcriptome for each disease-region combination. Scores (correlation coefficients) were considered statistically significant if they had an FDR-corrected correlation p value < 0.01.

SNP-to-gene mapping and gene level GWAS statistics

GWAS-linked gene enrichment analyses and disease susceptibility scoring was based on the van Rheenen et al. (Nature Genetics 2021) MetaBrain analysis.[59] GWAS summary statistics from this study were filtered and converted to standard format using the MungeSumstats R package.[101] We mapped SNPs to genes with MAGMA[100] and computed gene-level phenotype association statistics using a 10kb window up- and downstream of each gene.

Disease susceptibility scoring

We generated susceptibility scores using the single-cell disease relevance score (scDRS) python package.[102] Normalized and log-transformed counts from PN cases were used as input, with donor, sex, and unique gene counts as covariates. Genes were filtered to those expressed in >1% of cells. Cell scores were computed using the top 1000 most significant GWAS genes ranked by MAGMA Z score. The same genes were used for the differential enrichment analysis in Figure 4B. As this method is sensitive to sequencing depth and gene detection rate, raw scores were imputed using personalized PageRank[111] implemented in the ACTIONet R package before Z-scaling.

Differential enrichment analyses

Differential enrichment analyses of GWAS-linked genes (Figure 4B), disease and pathway-associated genes (Figures 4F, 5F, and S4C) were performed across all clusters using the Wilcoxon rank-sum test. We performed 100 trials of each test, randomly sampling 150 cells from each cluster per trial. We reported the Z scores of the mean LFCs and mean FDR-corrected p values across all trials.

CellPress

Supplemental figures

A **Demographics of profiled cohort**

	Cohort size	Sex	Region	Post-mortem interval	Age at death	Age at onset of symptoms	Survival after onset
Group	*n*	*n* M/F	*n* MCX/PFC	median (IQR), *h*	median (IQR), *y*	median (IQR), *y*	median (IQR), *y*
SALS	17	8/9	17/17	10.00 (7.00-15.00)	64.28 (60.29-71.62)	62.59 (55.98-69.80)	2.94 (1.42-3.67)
C9ALS	16	6/10	16/16	16.00 (9.75-27.00)	63.01 (59.75-67.96)	61.19 (57.64-65.33)	2.07 (1.91-3.00)
SFTLD	13	7/6	13/13	5.50 (4.50-10.50)	71.14 (69.50-74.04)	61.24 (58.45-64.15)	10.72 (9.02-12.42)
C9FTLD	11	6/5	10/11	6.00 (5.00-6.00)	75.00 (70.00-78.50)	65.96 (60.18-75.25)	8.50 (4.00-13.25)
PN	16	8/8	16/16	6.00 (5.12-15.75)	80.08 (63.49-84.97)	n/a	n/a

B **Post-filtering sample quality metrics by subtype**

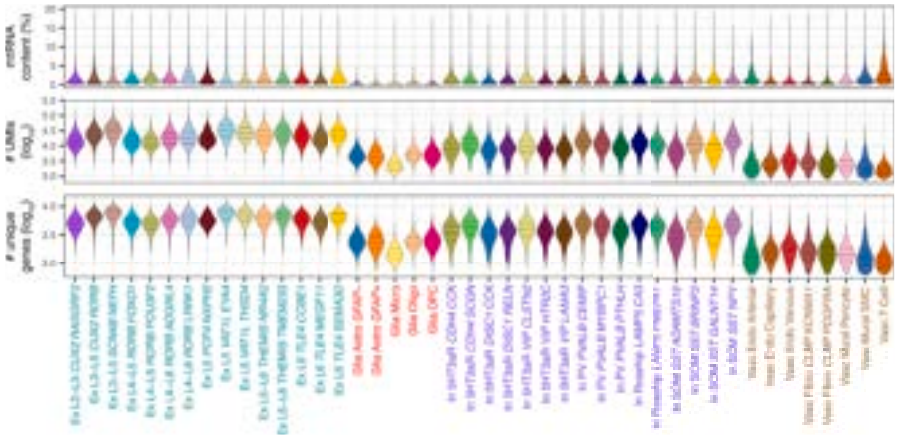

C Major cell class

D Major cell type

E Transcriptional subtype

L **Aggregation of subtypes for DEG analysis**

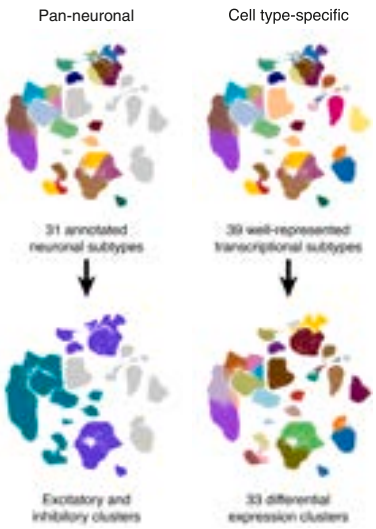

F Donor

G Sex

H Phenotype

I Genotype

J Brain region

K Bakken et al. (2021)

(legend on next page)

Figure S1. Cohort characteristics, data quality, and clustering annotations, related to Figure 1

(A) Summarized characteristics of profiled brain samples. Calculations include all individuals with available information: cohort size, sex, and region distribution, post-mortem interval (PMI), age of death, age of symptom onset, survival after onset; IQR: interquartile range; h: hours; y: years.

(B) Per subtype distributions of percentage of contaminant mitochondrial RNA (mtRNA; top), unique molecular identifier (UMI) counts (middle), and unique genes detected (bottom). Horizontal lines denote median and interquartile range values.

(C–J) UMAP clustering colored by (C) major cell class, (D) major cell type, (E) transcriptional subtype, (F) donor individual, (G) donor sex, (H) disease phenotype, (I) disease genotype, and (J) brain region. Colors in (E) correspond to those in (B), as well as to those in Figures 1A–1D.

(K) UMAP clustering colored by equivalent MCX annotations from Bakken et al. (Nature 2021).[73] These alternative annotations are provided in the annotated data. See STAR Methods.

(L) Aggregation of subtype clusters for DEG analysis (see Table S3; STAR Methods). Left: aggregation of neuronal subtypes into excitatory and inhibitory clusters for pan-neuronal DEG analysis. Right: aggregation of neuronal subtypes for cell-type-specific DEG analysis.

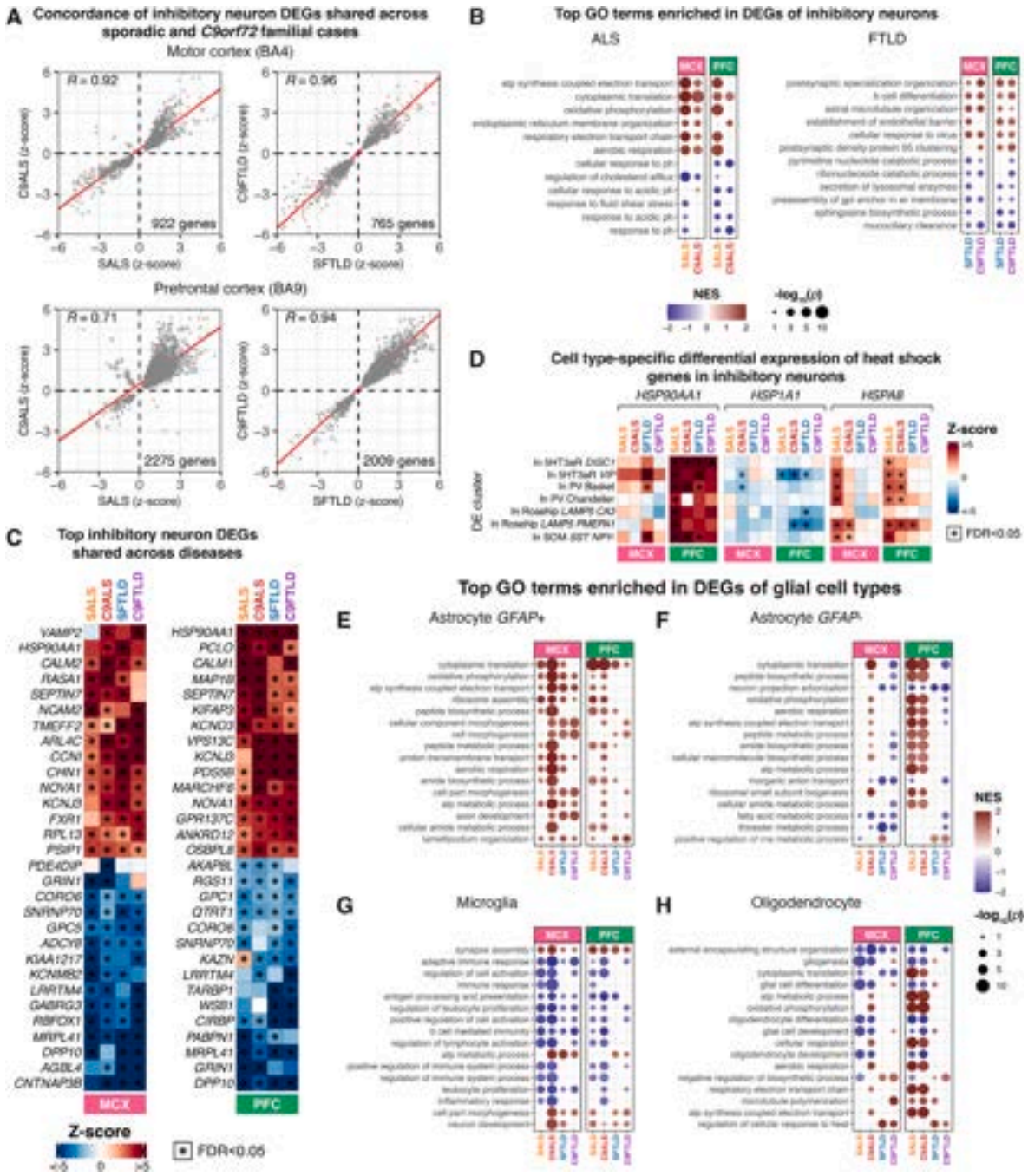

Figure S2. Gene expression changes in inhibitory and non-neuronal populations in ALS and FTLD, related to Figures 2 and 3

(A) Comparison of inhibitory neuron DEGs across genotypes. In each panel, the Pearson correlation is shown in the top-left, and the number of overlapping DEGs (FDR < 0.05 in both genotypes) is shown in the bottom-right.

(B) Select top-ranking GO terms enriched in DEGs of inhibitory neurons in ALS and FTLD cases.

(C) Top up- and downregulated genes shared across diseases in inhibitory neurons, per brain region.

(D) Differential expression of heat shock genes broadly dysregulated across inhibitory neurons. DE: differential expression.

(E–H) Top GO terms shared across diseases and brain regions in DEGs of (E) *GFAP*+ astrocytes, (F) *GFAP*− astrocytes, (G) microglia, and (H) oligodendrocytes.

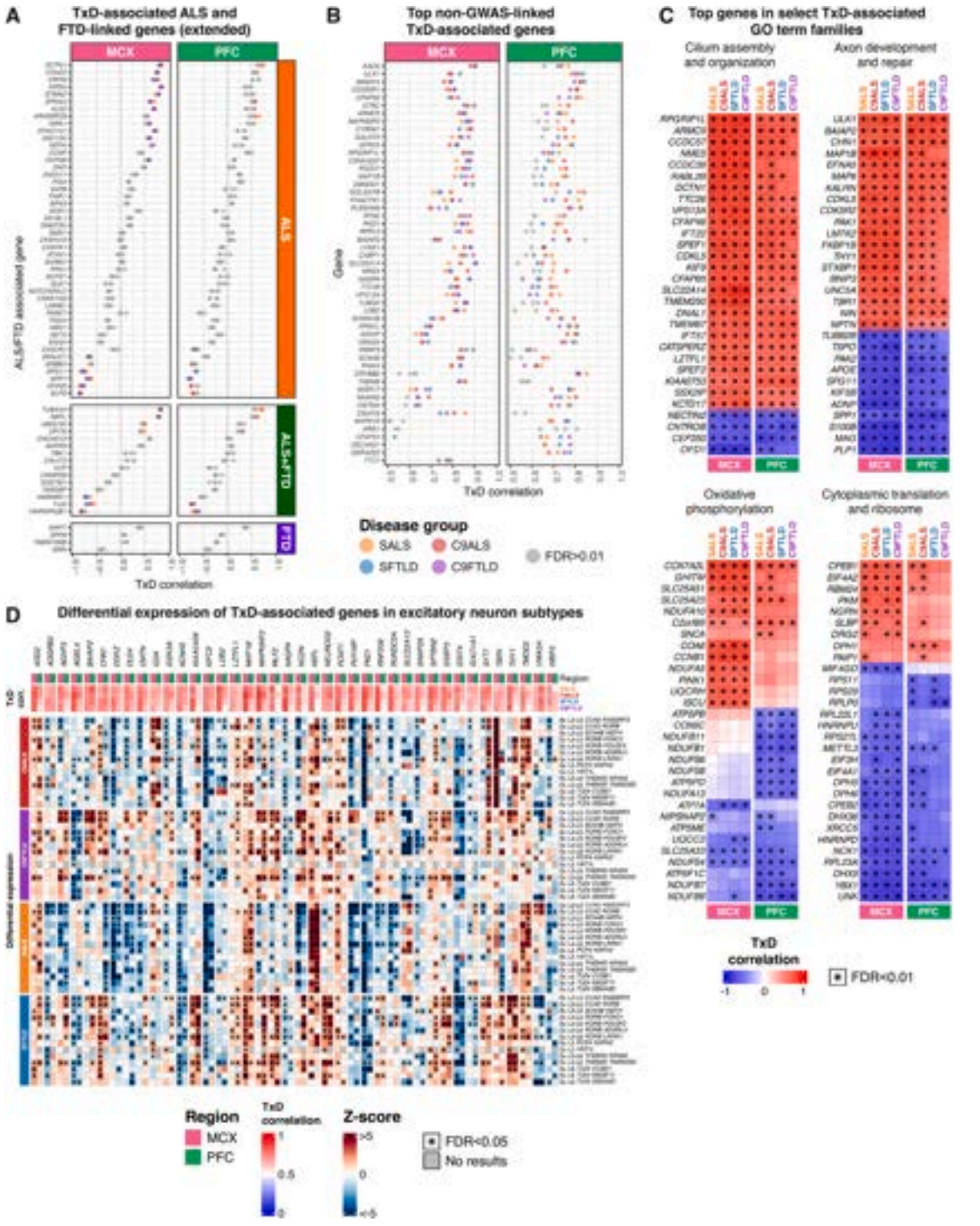

(legend on next page)

Figure S3. Drivers of cell-type-specific differential vulnerability, continued, related to Figure 4

(A) TxD association analysis of ALS- and FTD-linked genes. Extended version of Figure 4E.

(B) Top TxD-associated genes not previously genetically linked to ALS or FTD. Gray denotes not statistically significant. Combined legend for (A) and (B).

(C) Top-ranking genes in select overrepresented TxD-associated GO term families.

(D) Differential expression of top dysregulated TxD-associated genes. The top section represents the correlation of the TxD association. The bottom section shows the differential expression of each gene across diseases and brain regions.

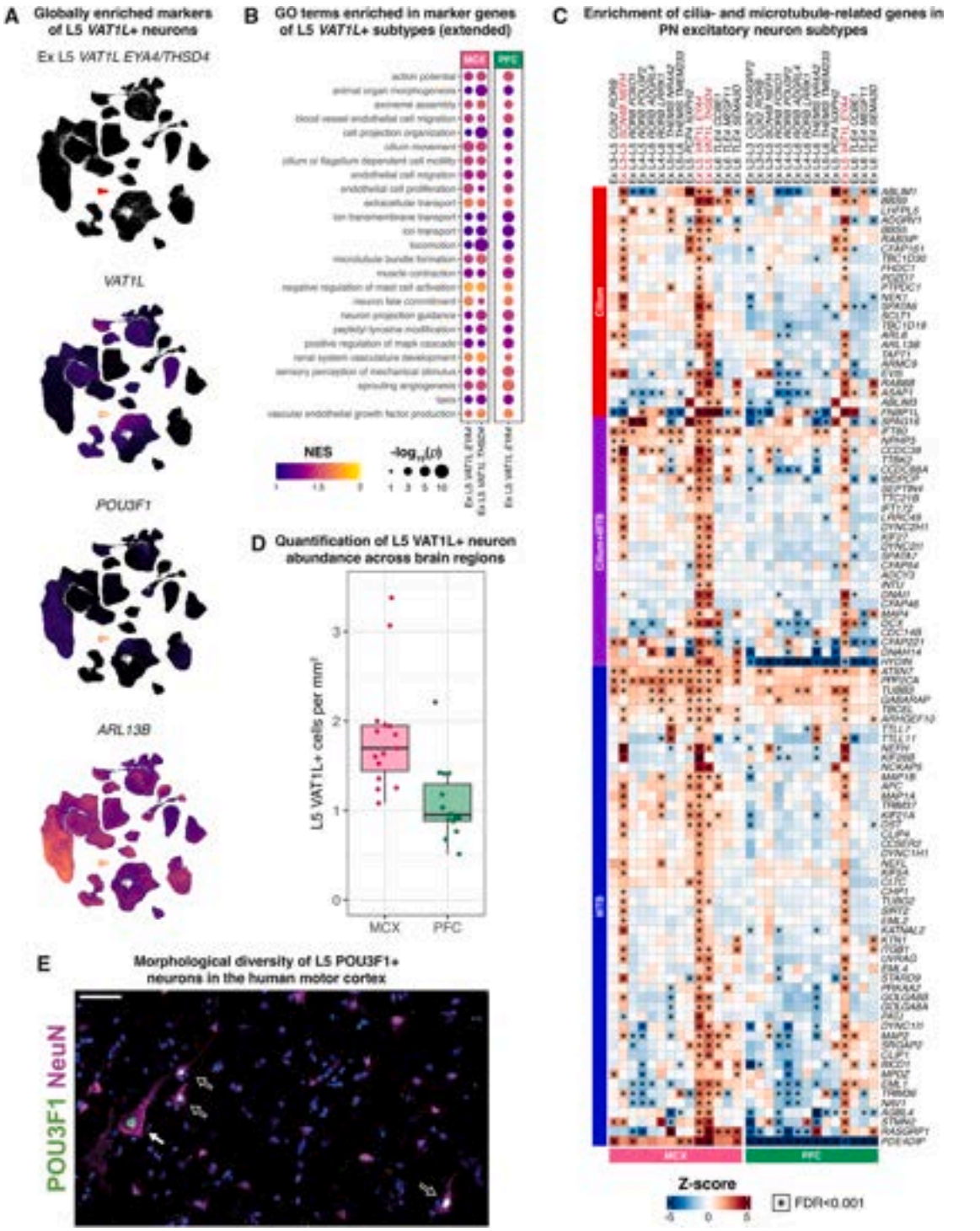

(legend on next page)

Figure S4. Characterization of vulnerable L5 excitatory populations continued, related to Figure 5

(A) UMAP heatmaps showing relative expression of select, globally enriched markers of differentially vulnerable L5 *VAT1L*+ neurons.

(B) Select top-ranking GO terms enriched in marker genes of human L5 *VAT1L*+ subtypes. Extended version of Figure 5E.

(C) Differential enrichment of cilia- and microtubule-associated genes across excitatory neuron subtypes. Differentially vulnerable subtypes are denoted in red. Extended version of Figure 5F.

(D) Histological quantification of VAT1L+ neuron density in L5 across brain regions of PN cases, irrespective of morphology.

(E) Representative image of immunofluorescent labeling of POU3F1 (green) and neuronal marker NeuN (magenta) in PN MCX. White arrow denotes a cell with Betz morphology, and the black arrows denote cells with non-Betz pyramidal morphology. Scale bars, 50 μm.

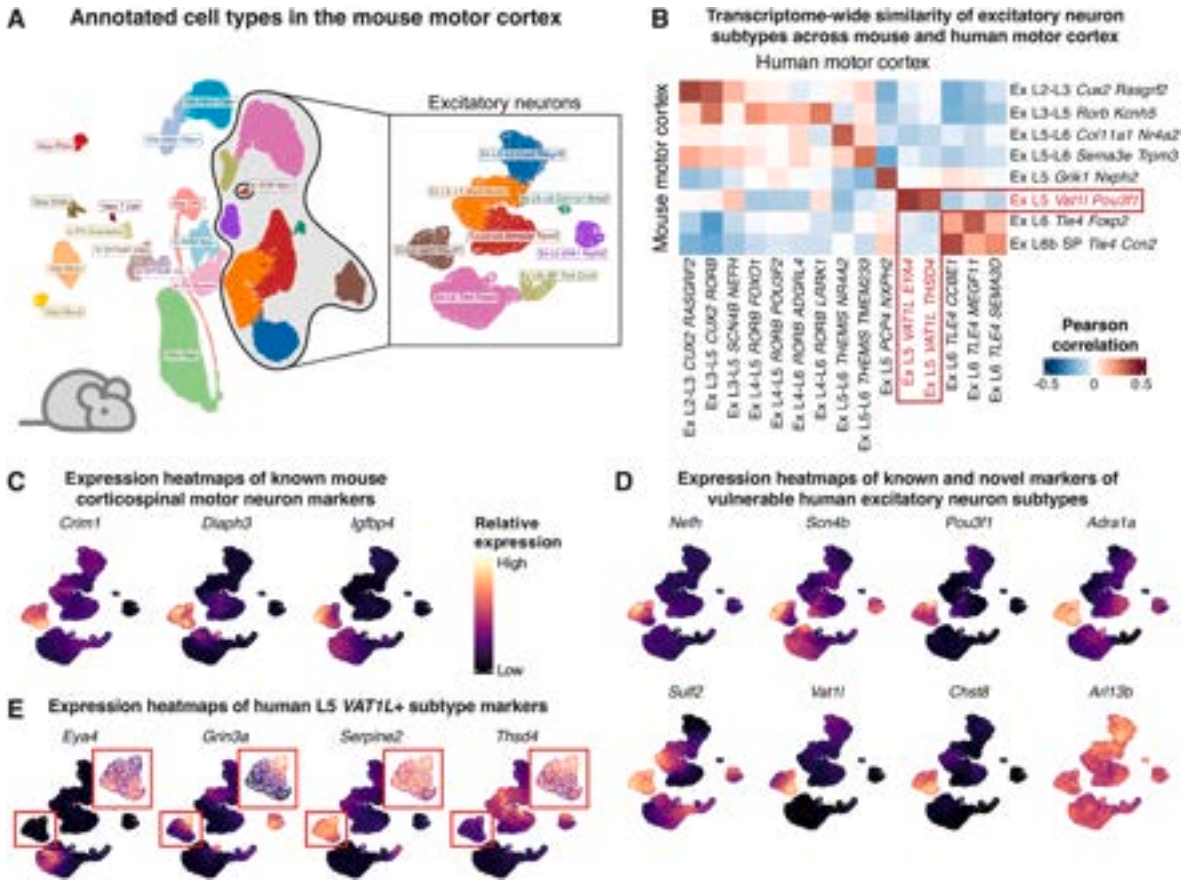

Figure S5. Identification and characterization of CSMN populations by homology to mouse primary motor cortex, related to Figure 5

(A) Annotated transcriptional subtypes in mouse MCX (45,206 cells). Inset: UMAP subplot of annotated excitatory neuron subtypes.

(B) Transcriptional similarity of excitatory neurons across human and mouse MCX. Putative UMN/CSMN-containing subtypes denoted in red.

(C–E) Heatmaps superimposed on the inset of (A) showing relative expression of (C) canonical mouse CSMN marker genes, (D) known and novel markers of differentially vulnerable excitatory neuron subtypes (from Figure 5B), and (E) markers that distinguish subtypes of L5 *VAT1L*+ neurons in human (from Figure 5B inset). Combined legend for (C)–(E).

A **Summary of VAT1L histological quantification results**

Cells counted	Region	vs. PN	Sample size *n* PN/disease	Cells in PN mean (cells/mm^2)	Cells in disease mean (cells/mm^2)	Change vs. PN (%)	*p*-value	Significance
All VAT1L+	MCX	ALS	15/26	1.83	1.28	-29.98%	0.003	**
		FTLD	15/18		1.66	-9.12%	0.186	ns
	PFC	ALS	15/26	1.08	1.00	-7.05%	0.279	ns
		FTLD	15/18		0.79	-26.45%	0.02	*
Betz only	MCX	C9ALS	15/12	0.19	0.05	-72.15%	0.00014	***
		SALS	15/14		0.05	-71.54%	0.00015	***
Non-Betz only	MCX	C9ALS	15/12	1.64	1.14	-30.61%	0.0068	**
		SALS	15/14		1.31	-20.32%	0.0351	*

B **Immunohistochemical staining of VAT1L in motor and prefrontal cortex L5**

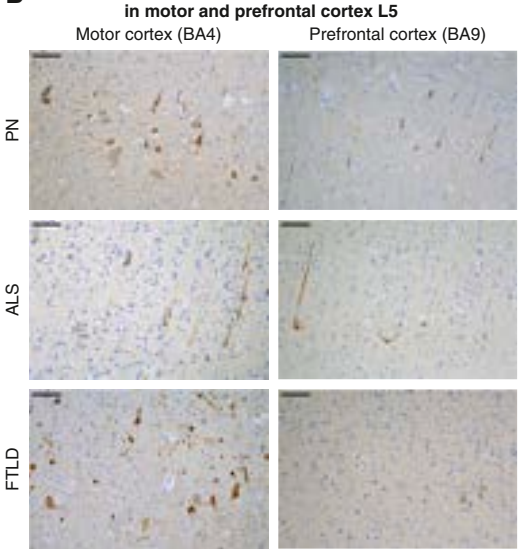

C **Top DEGs among overrepresented pathways in L3/5 *SCN4B+* neurons**

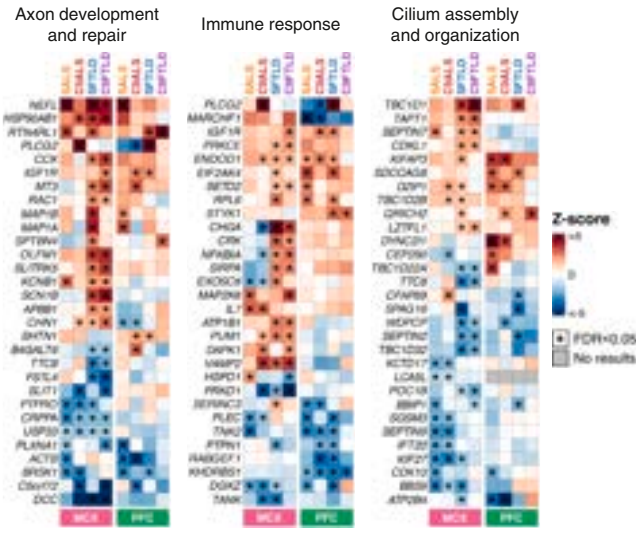

D **GO terms enriched in DEGs of L3/5 *SCN4B+* neurons**

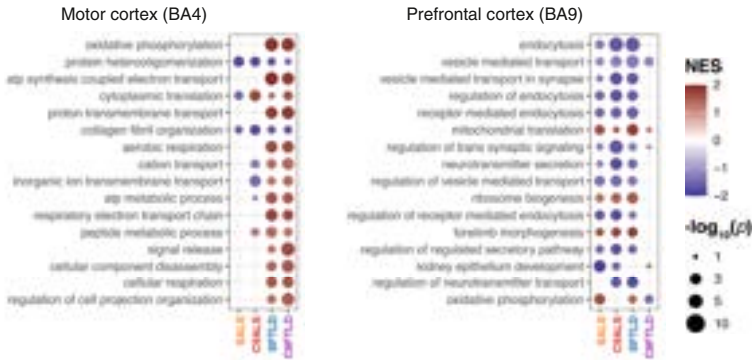

E **Top regulators of DEGs in L3/5 *SCN4B+* neurons**

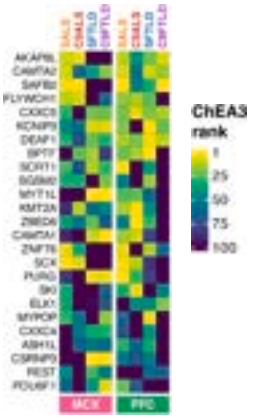

(legend on next page)

Figure S6. Impact of disease in differentially vulnerable cell types, continued, related to Figure 6

(A) Results of histological quantification of L5 VAT1L+ neuron loss. (*) $p < 0.05$; (**) $p < 0.01$; (***) $p < 0.001$; ns: not significant; one-tailed t test.

(B) Representative images of immunohistochemical labeling of VAT1L (brown) in motor and prefrontal cortex of PN, ALS, and FTLD cases used for stereological analysis of L5 VAT1L+ neuron depletion. Scale bars, 100 μm.

(C) Top DEGs of overrepresented GO term families enriched in L3/5 *SCN4B*+ neurons and shared with L5 *VAT1L*+ neurons.

(D) Enrichment of top-ranking GO terms in DEGs of L3/5 *SCN4B*+ neurons by brain region.

(E) Top-ranking ChEA3-predicted regulators of L3/5 *SCN4B*+ neurons DEGs. Values are the mean rank across ChEA3 libraries.